THERMOELECTRIC PROPERTIES OF NOVEL ONE-DIMENSIONAL AND TWO-DIMENSIONAL SYSTEMS BASED ON MoS_2 NANORIBBONS AND SHEETS

by

Abbas Arab

A Dissertation
Submitted to the
Graduate Faculty
of
George Mason University
In Partial Fulfillment of
The Requirements for the Degree
of
Doctor of Philosophy
Electrical and Computer Engineering

Committee:

_____	Dr. Qiliang Li, Dissertation Director
_____	Dr. Dimitrios Papacontantopoulos, Committee Member
_____	Dr. Dimitris Ioannou, Committee Member
_____	Dr. Rao Mulpuri, Committee Member
_____	Dr. Albert Davydov, Committee Member
_____	Dr. Monson Hayes, Department Chair
_____	Dr. Kenneth S. Ball, Dean, Volgenau School of Engineering
Date:_____	Spring Semester 2017 George Mason University Fairfax, VA

Thermoelectric Properties of Novel One-dimensional and Two-dimensional Systems Based on MoS2 Nanoribbons and Sheets

A Dissertation submitted in partial fulfillment of the requirements for the degree of Doctor of Philosophy at George Mason University

by

Abbas Arab
Master of Science
Sharif University of Technology, Tehran, Iran 2011
Bachelor of Science
Amirkabir University of Technology, Tehran, Iran 2009

Director: Qiliang Li, Associate Professor
Department of Electrical and Computer Engineering

Spring Semester 2017
George Mason University
Fairfax, VA

DEDICATION

To my wife and to my parents, without whom, none of this was possible.

ACKNOWLEDGEMENTS

I would like to thank my advisor, Prof. Qiliang Li, for his guidance and support during my graduate studies at George Mason University. His solid background in semiconductor materials and devices physics left a great impact on me. I truly appreciate the time and effort that Prof. Li has committed to the achievement of this work.

Special thanks to Dr. Dimitrios Papacontantopoulos, for his infinite patience and guidance during my research. He showed me the beauty of computational material science. A debt I cannot ever pay back.

I would like to express my gratitude to Dr. Albert Davydov, my supervisor at NIST for his tireless dedication to help and guide me.

I would like to thank Dr. Ioannou and Dr. Mulpuri for what I have learned from them during my research.

TABLE OF CONTENTS

Page

LIST OF FIGURES

LIST OF EQUATIONS

LIST OF ABBREVIATIONS

Transition metal dichalcogenides……...TMDC
Two-dimensional…….2D
Density Functional Theory……DFT
Non-Equilibrium Green's Function……NEGF
Two-Dimensional…….2D
One-Dimensional…….1D
Transition Metal Dichalcogenides……TMD
Chemical Vapor Deposition…….CVD
Armchair Nanoribbon……ACNR
Generalized Gradient Approximation…….. GGA
Local Density Approximation…….. LDA
Double Zeta Polarized……... DZP
Valence Band Maximum……. VBM
Conduction Band Minimum…… CBM

ABSTRACT

THERMOELECTRIC PROPERTIES OF NOVEL ONE-DIMENSIONAL AND TWO-DIMENSIONAL SYSTEMS BASED ON MOS2 NANORIBBONS AND SHEETS

Abbas Arab

George Mason University, 2017

Dissertation Director: Dr. Qiliang Li

Atomically thin materials such as hexagonal boron nitride (h-BN) and transition metal dichalcogenides (TMDCs) have attracted a lot of interest since the discovery of Graphene. Potential use of Graphene in semiconductor industry has been hindered by the fact that graphene is a semi metal with zero band gap. The difficulties in engineering band gap in graphene turn the focus light to inherent semiconducting two-dimensional (2D) materials; TMDCs.

Bulk of TMDCs are formed by layers vertically stacked and weakly bonded together via weak van der Waals interactions. These weak interlayer forces make it possible to obtain monolayer by using scotch tape exfoliation or lithium-ion intercalation. Among the semiconducting members of TMDCs, MoS_2 is the most appealing candidate, partly due to its thermal stability and also for its natural abundance. Intensive study of electronic properties of MoS_2 has revealed the desirable band gap (1.2 eV), good carrier

mobility (which is close to those of silicon thin films and graphene nanoribbons), thermal stability and a surface free from dangling bonds make it a perfect candidate for electronic and opto-electronic applications. Despite the fact that MoS_2 has a high Seebeck coefficient, its thermoelectric properties have not studied as well as it should be.

In this work, we have studied thermoelectric properties of monolayer and fewlayer MoS_2 sheets in both armchair and zigzag orientations and also of monolayer MoS_2 armchair nanoribbons. Density functional theory (DFT) using non-equilibrium Green's function (NEGF) method in ballistic transport regime of Landauer-Buttiker formulation in linear transport approximation has been implemented to calculate the transmission spectra and consequently electronic transport coefficients. Phonon transmission spectra are calculated based on parameterization of Stillinger-Weber potential. Thermoelectric figure of merit, ZT, is calculated using these electronic and phonon transmission spectra.

In the case of MoS_2 sheets, thermoelectric properties of monolayer, bilayer, trilayer and quadlayer in armchair and zigzag directions have been studied. Our results show that as number of layers increase from monolayer to quadlayer, both transmission spectrum and phonon thermal conductance increase. In addition, strong electronic and thermal anisotropy is found between zigzag and armchair orientations. Transmission coefficient and phonon thermal conductance of zigzag orientation is higher than those of armchair with the same number of layers. Electrical conductance and phonon thermal conductance are competing forces in achieving a high thermoelectric figure of merit. Advantage of having a higher electrical conductance in zigzag orientation has been nullified by having a higher phonon thermal conductance. In fact, our results show higher thermoelectric

figure of merit for armchair oriented than zigzag oriented sheets. Also as number of layer decreases from quadlayer to monolayer, we are witnessing a higher thermoelectric figure of merit for both armchair and zigzag oriented sheets. Hence, the highest achieved thermoelectric figure of merit was obtained by monolayer armchair MoS_2 sheet for both p-type and n-type semiconducting behavior.

In case of MoS_2 armchair nanoribbons, effect of several factors has been studied; width of nanoribbon, Sulfur vacancy and edge roughness. The electronic properties of nanoribbons are dominated by the presence of edge states that are dependent on the number of zigzag chains across the nanoribbon. In addition, it is found that the phonon thermal conductance of monolayer MoS_2 armchair nanoribbon is smaller compared to MoS_2 monolayer armchair sheet. This outcome can be explained by phonon edge scattering. The effect of this phonon edge scattering is more pronounced in narrower nanoribbons compared to wide ones which leads to higher thermoelectric figure of merit for narrow nanoribbons. The effect of edge roughness and sulfur vacancy on thermoelectric behavior of MoS_2 nanoribbons is also studied. Our result shows that edge roughness decreased the thermoelectric figure of merit compared to those of a perfect nanoribbon as its impact on electrical conductance is more severe than on phonon thermal conductance. Sulfur vacancy, however, improved thermoelectric figure of merit of MoS_2 nanoribbons. It has been shown that thermoelectric figure of merit as high as 4 and 3 at $T = 500K$ can be achieved n-doped and p-doped MoS_2 nanoribbons. The ability of getting a high thermoelectric figure of merit for both n-type and p-type behavior from the same material will be a huge boost to thermoelectric industry if realized.

CHAPTER ONE: INTRODUCTION

1.1 Overview of Solid State Thermoelectric Materials

Providing a sustainable source of energy in 21st century in which fossil fuels are decreasing and demand for energy is increasing every moment will be a major challenge. Thermoelectric phenomena which involves conversion between heat and electrical energy and provide a method to heat and cool materials or generate electricity from wasted heat sources have been supposed to have a significant role in meeting energy challenges. As a result, we expect an increasing emphasis on developing advanced thermoelectric materials.

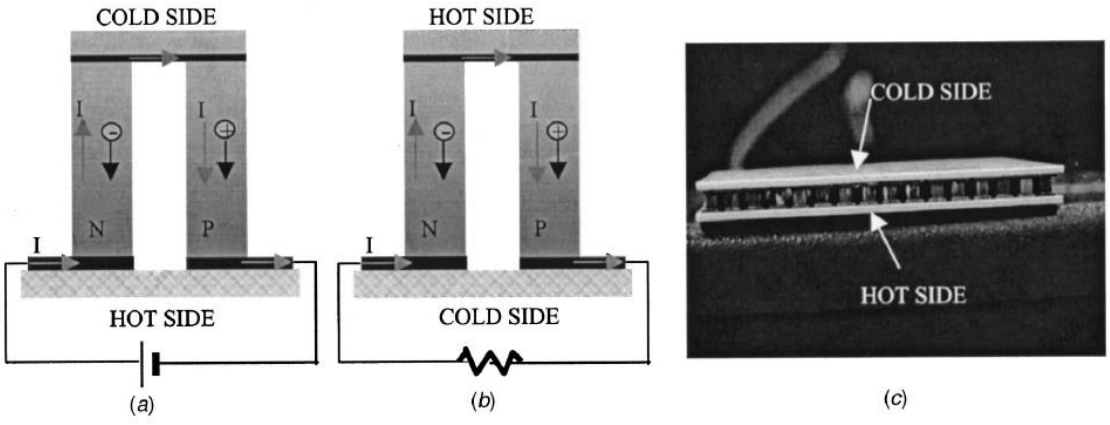

Figure 1.1 Thermoelectric devices; a) cooler, b) power generator and c) an actual

As charge carriers transfer in conductor and semiconductor materials, they also transport energy. Consider Fig. 1.1(a), the connection of a p-type and an n-type semiconductor legs electrically in series and thermally in parallel is called a thermocouple. As you can see in this figure top side of the semiconductors are contacted by a cold source and the other side is contacted by a hot source and the whole system is biased by a constant electrical potential. This electric bias forces the current to pass through the semiconductor legs in thermocouple. Electrons in n-type leg and holes in p-type leg carry the current as depicted in Fig. 1.1(a). This transport of carriers from top side to bottom side will carry thermal energy away from the top side and hence cooling the top side. This effect is known as Peltier effect. Conversely, as shown in Fig 1.1(b), if a thermal gradient is held across the thermocouple, electrons and holes with higher thermal energy in n-type and p-type semiconducting leg, respectively, will diffuse toward the side with lower thermal energy. This diffusion of carriers from hot side toward cold side will continue until a net potential barrier develops and an equilibrium between charge diffusion and repulsion will be achieved. The magnitude of this potential barrier is known as Seebeck coefficient. Peltier effect and Seebeck effect are the backbone and fundamental effect of solid state cooling and power generation.

Thermoelectric devices contain many thermocouples made of an n-type and a p-type material wired thermally in parallel and electrically in series, see Fig. 1.2. A thermoelectric generator uses heat flow across temperature gradient to power electrical load through the external circuit. The temperature difference provides the voltage through Seebeck effect.

The field of thermoelectrics advanced rapidly in 1950s when the basic science of thermoelectricity became formulated and established, thermoelectric material Bi_2Te_3 was developed for commercialization and hence launching thermoelectric industry. It was already established by that time that the effectiveness of a thermoelectric material could be approximately linked to a dimensionless thermoelectric figure of merit: $ZT = GS^2T/\kappa$ in which G,S, T and $\kappa = \kappa_e + \kappa_{ph}$ are electrical conductance, Seebeck coefficient, absolute temperature and thermal conductance which comprise of electronic (κ_e) and phonon (κ_{ph}) components[1]. Over the following three decades, thermoelectrics field received little interest from research communities. Nevertheless, it was improving slowly

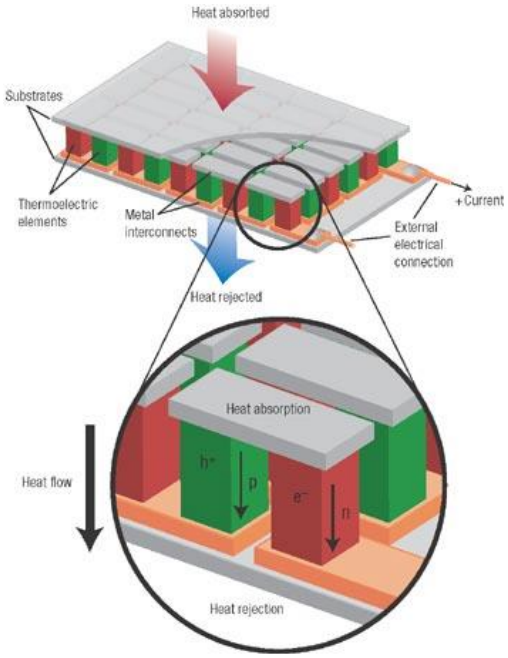

Figure 1.2: Schematic of thermoelectric module, each module contains many thermocouples connected thermally in parallel and electrically in series.

and steadily. In the 1990s, Department of Defense stimulated research communities to be active in this field once again and find innovative ways to improve the efficiency of solid state cooling and power generation. As a result of this initiative two different approaches were taken for developing the next generation of thermoelectric materials; one using a new family of bulk materials[2–4] and the other using low-dimensional material systems[5].

The advanced bulk material approach focused on decreasing thermal conductance of the material. Total thermal conductance of any material can be broken down to two components; electronic contribution and phono contribution. Electronic contribution of thermal conductance can be calculated from its electrical conductance using Wiedmann-Franz law. Lattice or phonon thermal contribution can usually be understood by material lattice structure. Materials with large unit cells, disorders and variety of atom types are known to scatter phonons and have low lattice thermal conductance. At the extreme, glasses and amorphous materials in general, have the highest phonon scattering rate with mean free path ranging down to atomic distances. But, amorphous materials scatter electrons as well and hence decrease the electrical conductance. As a result, a perfect material for thermoelectric purposes is a material that acts as a glass for phonons, meaning to have the maximized phonon scattering rate, and also acts as a crystal for electrons. These criteria are well known as "Electron Crystal, Phonon Glass"[4]. A perfect example of these prototype materials is partially filled Skutterudites based on alloys of $CoSb_3$[6]. Lattice structure of filled Skutterudites for $LaFe_3CoSb_{12}$ has been illustrated in Fig. 1.3 in which large and heavy La atoms serve as a rattler. The effect of introducing this rattler atom is depicted in Fig. 1.4. On the left hand panel, refined atomic

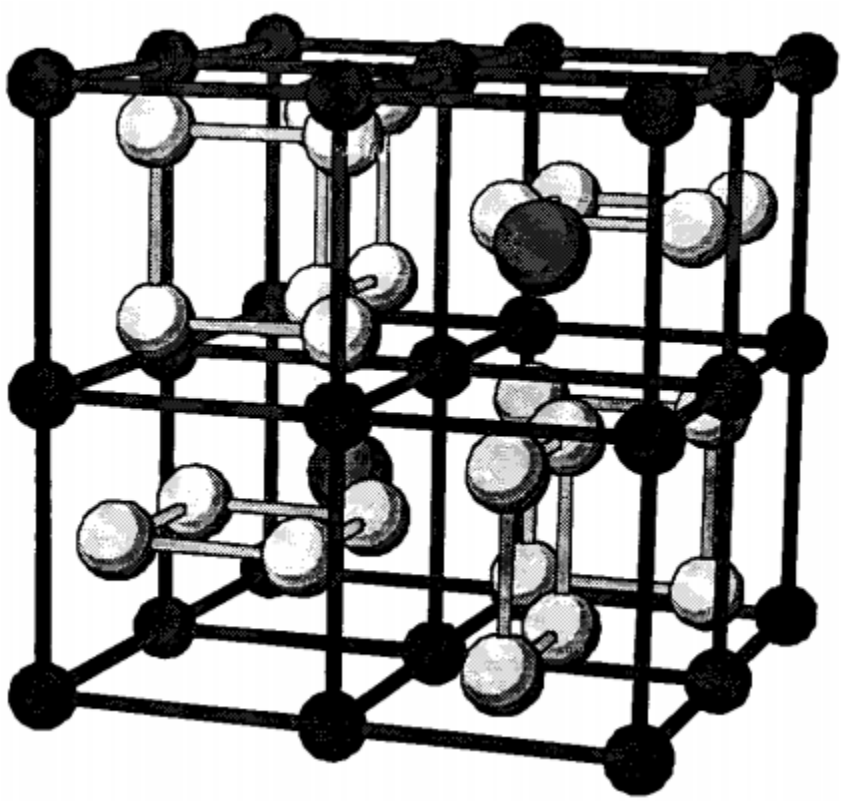

Figure 1.3: Lattice structure of partially filled Skutterudites for $LaFe_3CoSb_{12}$, the two large dark spheres represent the La atoms, small dark spheres represent Fe or Co atoms and small light spheres represent Sb atoms. Large and heavy guest La atoms into the structure is introduced into the structure to serve as a rattler in order to increase phonon scattering and hence reduce lattice thermal conductance.

displacement of atoms in the material has been plotted using a four-cycle neutron diffractometer. La, the rattler atom, has shown higher atomic displacement parameter with respect to the other atoms. The effect of this higher atomic displacement on lattice thermal conductance of the whole system is illustrated in right hand panel of Fig. 1.4. Lattice thermal conductance of $CoSb_3$, $CeFe_4Sb_{12}$ and $LaFe_3CoSb_{12}$ versus temperature is plotted. As you can see introducing La atom in the lattice structure the lattice thermal

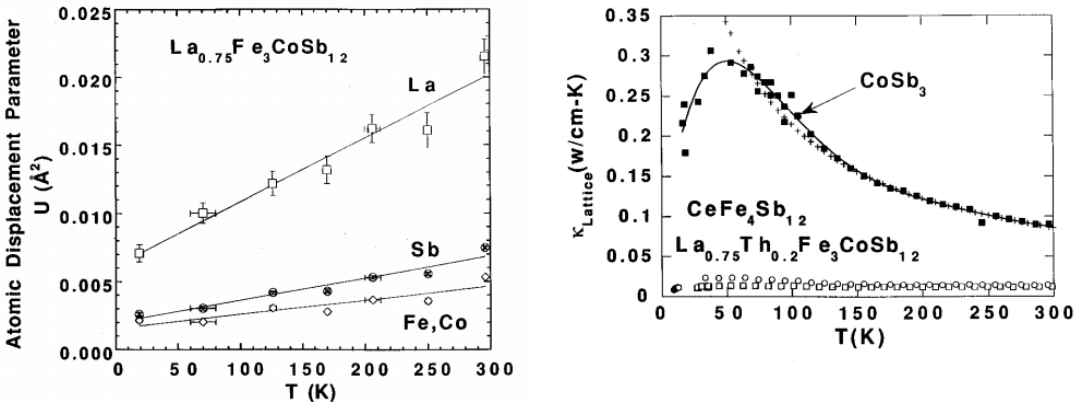

Figure 1.4 (left panel) atomic displacement parameter from a four-cycle neutron diffractometer for partially filled Skutterudites, broken down for different atomic species. (right panel) lattice thermal conductance for ceramic $CoSb_3$, unfilled Skutterudites $CeFe_4Sb_{12}$ and filled Skutterudites $La_{0.75}Th_{0.2}Fe_3CoSb_{12}$.

conductance of the filled Skutterudites to be more than six times lower than of ceramic $CoSb_3$.

As mentioned above, the other direction that research communities followed in order to develop a high-ZT material was using low-dimensional structures. In conventional bulk materials, parameters that are affecting the ZT are interrelated. In other words, by trying to increase the Seebeck coefficient for example, you will decrease the electrical conductance and consequently electronic thermal conductance. As a result, there would be no net impact on ZT. However, by reducing the dimensionality of the system and moving toward nano-scale systems a new factor of length scale will become available in order to control the material properties. As length scale of the system decreases and approaches nanometer scale, dramatic variation in density of states is possible allowing to vary material characteristics affecting the ZT quasi-independently.

Field of low-dimensional thermoelectric materials was introduced by two novel ideas to boost ZT. The first approach was to take advantage of quantum confinement to increase Seebeck coefficient and control Seebeck coefficient and electrical conductance independently. The other approach was to decrease phonon thermal conductance by introducing many interfaces in the system and to be able to scatter phonons more effectively than electrons[7]. An example of first approach in low-dimensional thermoelectric materials, increasing Seebeck coefficient via quantum confinement, is PbTe/PbSe quantum dot super lattices. Because of lattice mismatch between PbTe and PbSe, attempting to grow a thin layer of PbSe on top of PbTe, would result to formation of ordered arrays of PbSe quantum dots sandwiched between PbTe layers, following the Volmer-Weber process[8,9]. Such a quantum dot sandwiched super lattice has been realized by Harman et al[10–12]. Super lattice structures over a thousand periods of composition $PbSe_{0.98}Te_{0.02}$ on top of BaF_2 substrate and a thin $PbTe$ buffer has been grown. Using Bi as n-type dopant for this quantum dot super lattice, ZT values as high as 1.6 and 3.5 have been achieved at T = 300 K and T = 500 K, respectively[12]. The schematic of this super lattice as well as measured ZT values versus temperature have been illustrated in Fig. 1.5.

The other approach in low-dimensional thermoelectric material approach was to decrease lattice thermal conductivity by introducing many interfaces in the material to increase the phonon scattering. This introduction of many interfaces in the material should be designed so that the reduction in electrical conductance caused by them should be compensated more than by decrease in decrease in lattice thermal conductance.

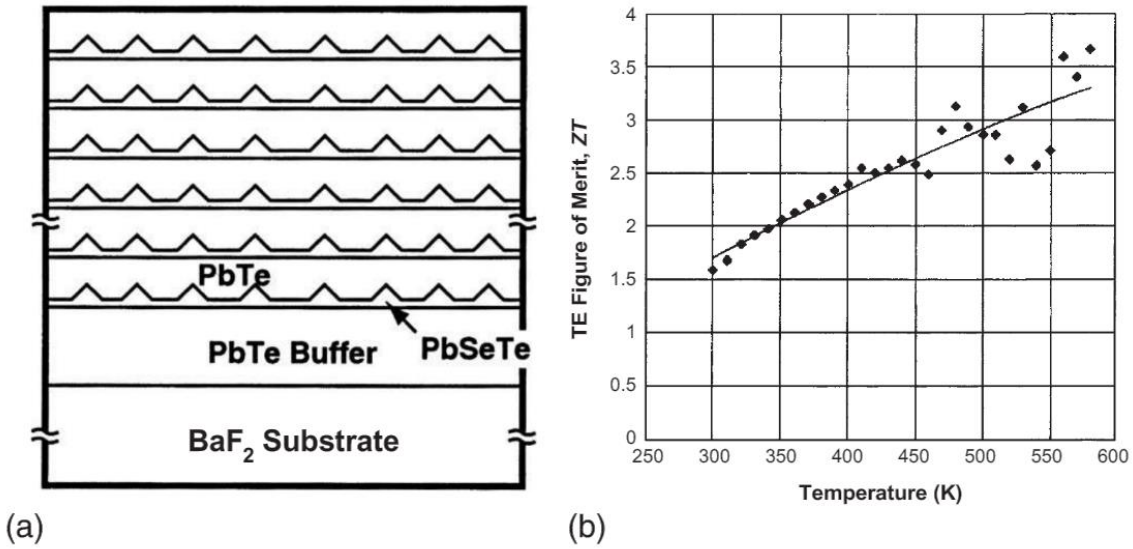

Figure 1.5: (a) Schematic of PbTe/PbSe quantum dot super lattice and (b) Thermoelectric figure of merit for a $PbSe_{0.98}Te_{0.02}/PbTe$ quantum super lattice doped by Bi atoms.

Thermal conductivity reduction is the main strategy for improving thermoelectric properties in super lattice systems. Past studies have shown that periodicity in super lattices does not have any effect on the performance of the thermoelectric materials. As a result, nanocomposite materials became the natural next step to pursue improvements in thermoelectric materials[13]. Model calculations provide a significant role in designing the parameters in fabricating the nanocomposite materials. Decrease in lattice thermal conductance of nanocomposite materials in comparison to their bulk alloy samples with the same nominal composition of constituents is the main goal in designing nanocomposite thermoelectric materials. Model calculations can guide us in designing fabrication parameters in nanocomposite materials.

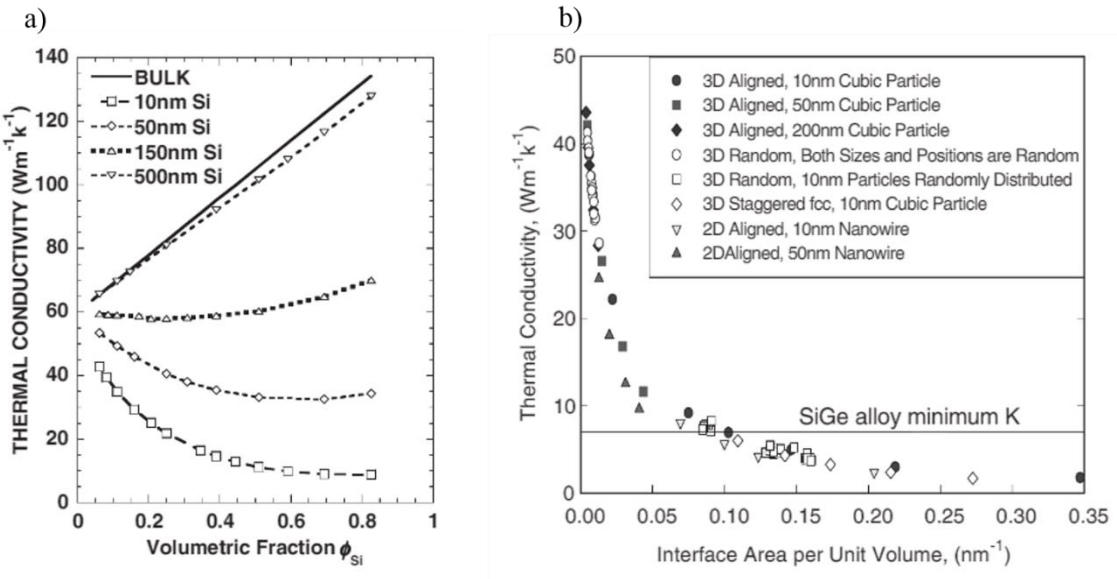

Figure 1.6: a) Calculated thermal conductivity vs. increasing silicon fraction for Si_xGe_{1-x} nanocomposite material. (b) Monte-Carlo simulation of Si_xGe_{1-x} for different alignments of nanoparticle in nanocomposite materials.

The results of two model calculations are illustrated in Fig. 1.6. In panel (a) of Fig. 1.6, lattice thermal conductivity of Si_xGe_{1-x} in form of alloy and also a nanocomposite material of Ge host consisting of Si nanoparticles has been compared. As it can be seen lattice thermal conductance of bulk alloy as well as the nanocomposite material that contains nanoparticles of cross-sectional width size of 500nm keeps increasing by increasing the nominal composition of silicon in the material reflecting higher sound velocity in silicon than in germanium. For nanocomposite material containing silicon nanoparticles with cross-sectional width size less than 50nm, there will be a decrease in lattice thermal conductance by increasing the silicon volumetric fraction. The reason for this behavior is that for nanocomposite materials with nanoparticles with small width

size, the mean free path is limited by nanoparticle width size. As a result, lattice thermal conductivity becomes more sensitive to velocity of sound and specific heat rather than to bulk mean free path of scattering. In this regime, nanocomposite materials with nanoparticles in less than 50nm in width, lattice thermal conductance decreases by increasing the silicon volumetric fraction. This is in contrast to what happens in bulk alloy samples. The reason for this behavior is that, lattice thermal conductance of silicon nanoparticles suffers more from interface scattering than any other factor. By increasing the silicon volumetric fraction in the nanocomposite material, we are introducing more interfaces and at the same time the role of silicon in determining thermal conductance of the system is increasing. As a result, the lattice thermal conductance of the whole system decreases. Panel (b) of Fig. 1.6, illustrates Monte-Carlo simulation of nanocomposite materials with different size and alignment strategies and compare their lattice thermal conductance to the bulk alloy[14]. It can be seen that the effect of introducing interfaces in the nanocomposite materials is independent of how you introduce them. This fact opens the door for investigating the self-assembled nanoparticles and their potential use in thermoelectric industry.

By far the most widely commercially used thermoelectric materials are alloys of Bi_2Te_3 and Sb_2Te_3. For near-room-temperature applications, such as refrigeration and waste-heat recovery, Bi_2Te_3 alloys have been proved to possess the greatest figure of merit for both n- and p-type thermoelectric systems. Bi_2Te_3 was first investigated as a material of great thermoelectric promise in 1950s[15]. It was quickly realized that alloying with Sb_2Te_3 and Bi_2Se_3 allowed for fine tuning of carrier concentration alongside a

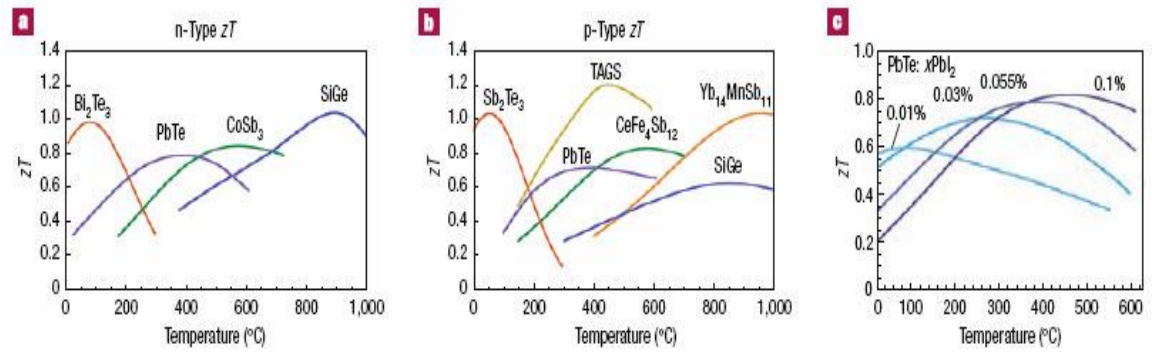

Figure 1.7: Figure of merit ZT of state-of-the-art commercial materials and those or being developed for thermoelectric generation. (a) and (b) for n- and p-type, respectively. Most of these materials are complex alloys and approximate composition is shown. (c) Altering doping concentration changes not only the ZT peal value but also the temperature at which the peak occurs.

reduction in lattice thermal conductivity. The most commonly studied p-type compositions are near $(Sb_{0.8}Bi_{0.2})_2Te_3$ whereas n-type compositions are close to $Bi_2(Te_{0.8}Se_{0.2})_3$. Peak ZT of these materials are usually in the range of 0.8 to 1.1 with p-type materials achieving highest values. By adjusting carrier concentration ZT can peak at different temperature enabling the tuning of the materials for specific applications[16]. For mid-temperature power generation (500-900K), materials based on group-IV tellurides are typically used , such as PbTe, GeTe or SnTe[17,18]. The peak ZT value in optimized n-type materials is about 0.8. Successful high-temperature (>900K) thermoelectric generators have typically used Silicon-Germanium alloys for both n-type and p-type legs. The ZT of these materials are fairly low, particularly for p-type materials because of relatively high lattice thermal conductivity of the diamond structure. ZT figure

of merit of the state-of-the-art commercialized thermoelectric materials is illustrated in Fig. 1.7.

1.2 MoS_2 as a New Low-Dimensional Material

Atomically thin two dimensional (2D) materials have attracted a strong interest since the discovery of Graphene[19]. Great strides have been made toward understanding its interesting physical and electrical properties[20,21]. However, Graphene's potential use in electronics application has hindered by the fact that it has zero band gap in its pristine form. More recently, another family of 2D materials has emerged; transition metal dichalcogenides (TMDs). Crystal of these materials is formed by layers vertically stacked and weakly bonded together via van der Waals forces. Each layer is formed by a plane of transition metal atoms sandwiched between two planes of chalcogen atoms in trigonal prismatic arrangements as illustrated in Fig. 1.8. This weak interlayer interaction makes it possible to extract monolayer by using scotch tape exfoliation[22] or lithium-ion intercalation[23] techniques. In contrary to zero band gap of Graphene, some members of TMD family have an appropriate band gap for microelectronic applications. Among those, molybdenum disulfide (MoS_2) is the most representative, widely interesting and intensively studied one, in part due to its thermal stability and natural abundance[24–26]. Bulk MoS_2 is an indirect semiconductor[27] with a band gap of 1.2 eV, whereas monolayer MoS_2 is a direct semiconductor[28] with a band gap of 1.8 eV. This desirable band gap, carrier mobility close to that of Silicon thin films and graphene nanoribbons[29], excellent thermal stability and a surface free from dangling bonds[30], make MoS_2 a promising candidate for electronic and optoelectronic applications[31].

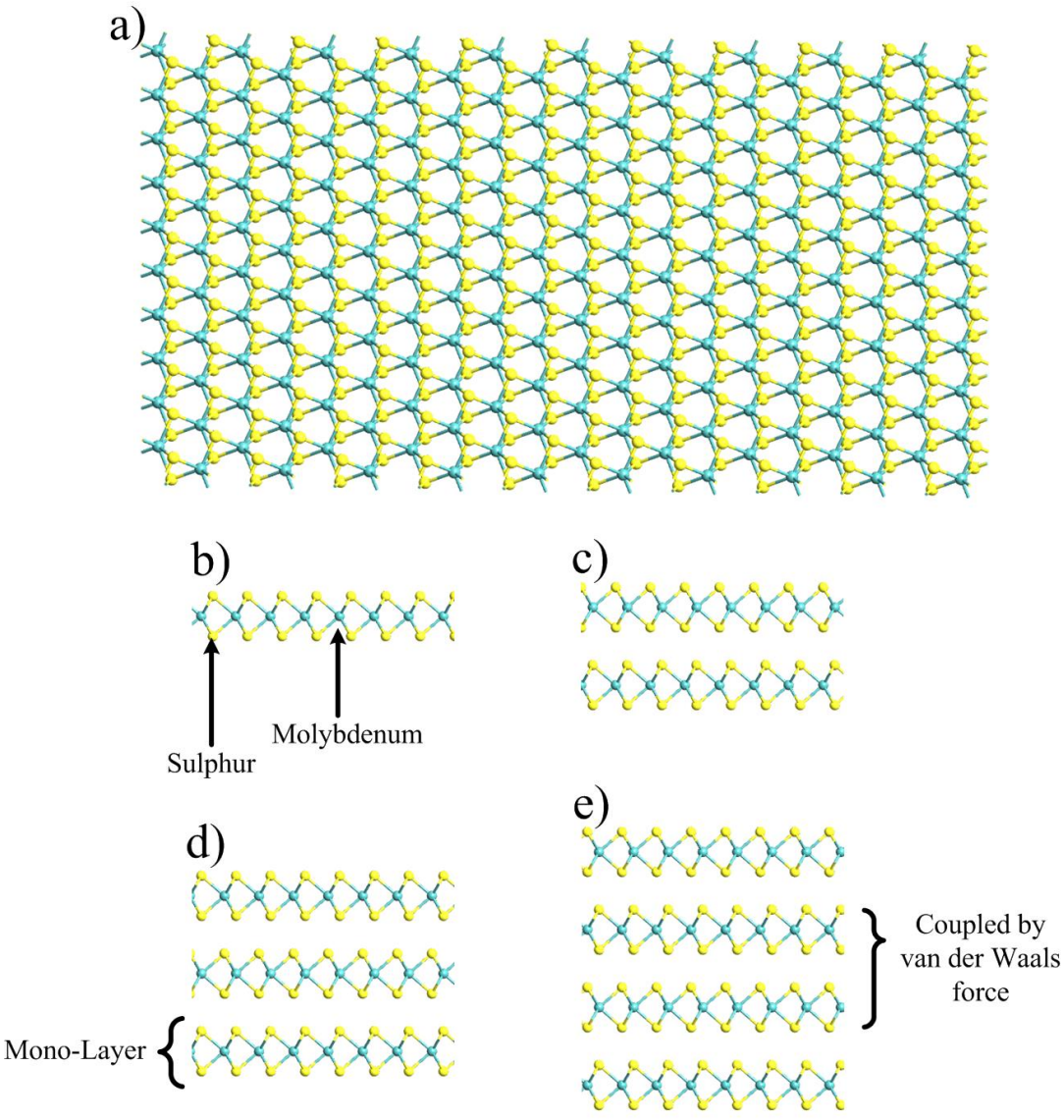

Figure 1.8: Atomic structure of MoS_2. (a) Monolayer of MoS_2 is made of a honeycomb sheet of Molybdenum atoms covalently sandwiched between two honeycomb sheets of Sulphur atoms. Bulk of MoS_2 is formed by monolayers stacked and held on top of each other by van der Waals forces. Side view of mono-, bi-, tri- and quadlayer is illustrated in parts (b), (c), (d) and (e), respectively.

Thermoelectric properties of MoS_2 is not studied as well as its electrical and

mechanical properties[32,33]. Direct conversion of heat to electricity in thermoelectric materials, is considered to be an interesting resolution to energy shortage problem and hence search for a highly efficient thermoelectric material has attracted strong interest in material science. In thermoelectric materials, it is desirable to have a high electrical conductance and Seebeck coefficient and low thermal conductance to achieve a high ZT value. In conventional thermoelectric materials, i.e. PbTe[34] and Bi2Te3 based alloys[35], ZT values around 2.4 at $T = 900K$ have been already achieved. Further increase in ZT of these materials proved to be a challenge since parameters that affect ZT, are generally coupled with each other. Enhancement to one of them may degrade the other and overall effect on ZT will neutralize. The situation became more promising since it was suggested that low-dimensional[36,37] and nanostructured thermoelectric materials[38] can exhibit higher ZT value based on increase in Seebeck coefficient caused by quantum confinements and also decrease in thermal conductance caused by increased phonon boundary scattering[39]. Thermal conductivity can be decreased even more by deliberately introducing surface roughness[40] and defects in material[41].

High Seebeck coefficient of $600\,\mu V/K$ at room temperature[42] is reported for bulk MoS_2 which is higher than most of good thermoelectric materials. Back in 1950s, Mansfield and Salam[42], showed that bulk MoS_2 possess a high Seebeck coefficient, a required characteristics for high performing thermoelectric materials. During a Hall effect measurement, they have passed a steady current through the sample and measure the Hall voltage using a potentiometer. They kept track of the potential before and after turning on a magnetic field. This procedure was repeated several times and for different period of

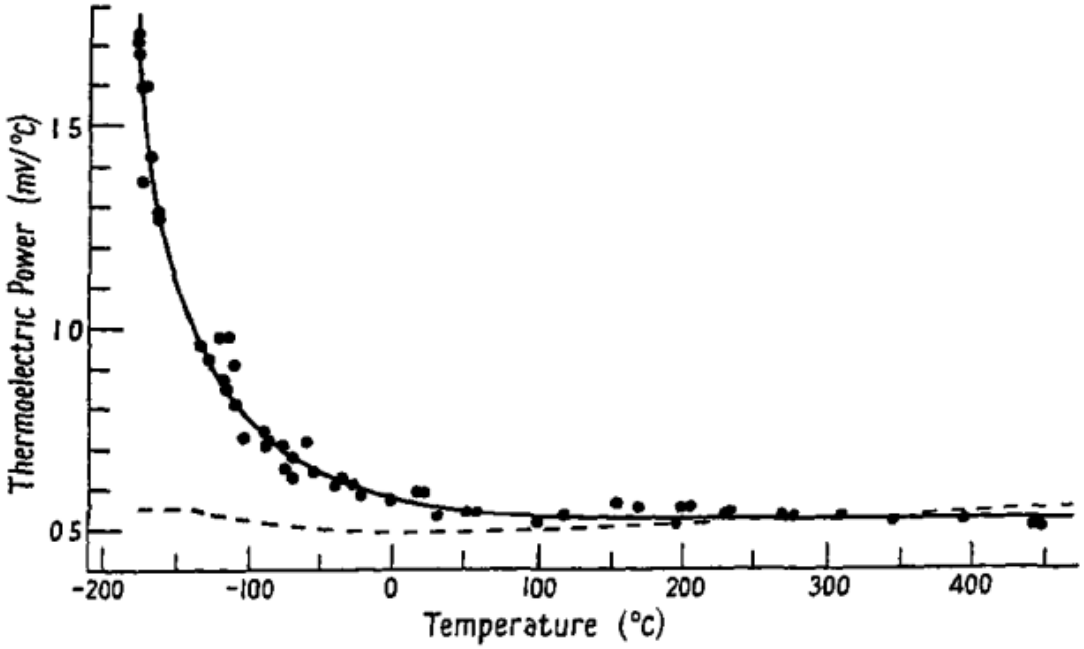

Figure 1.9: Seebeck coefficient (also known as thermoelectric power) of MoS_2 measured by Mansfield and Salam back in 1950s.

time that magnetic field was on. The presence of Ettingshausen effect, causes inducing a temperature gradient across the Hall probes which consequently induced some voltage, Seebeck effect. They managed to measure the voltage induced by temperature gradient per unit temperature increase, which is Seebeck coefficient. Their result is illustrated in Fig. 1.9.

It is also shown that Seebeck coefficient of MoS_2 can be tuned as high as $10^5\ \mu V/K$ by imposing a gate electric field. Buscema et al.[43] used a monolayer MoS_2 flake obtained by mechanical exfoliation and deposited on Si/SiO_2 substrate. Electrical contacts of 5nm titanium and 50nm gold has been deposited by standard electron beam deposition techniques to serve as an ohmic contact. Then with zero bias, all electrodes grounded,

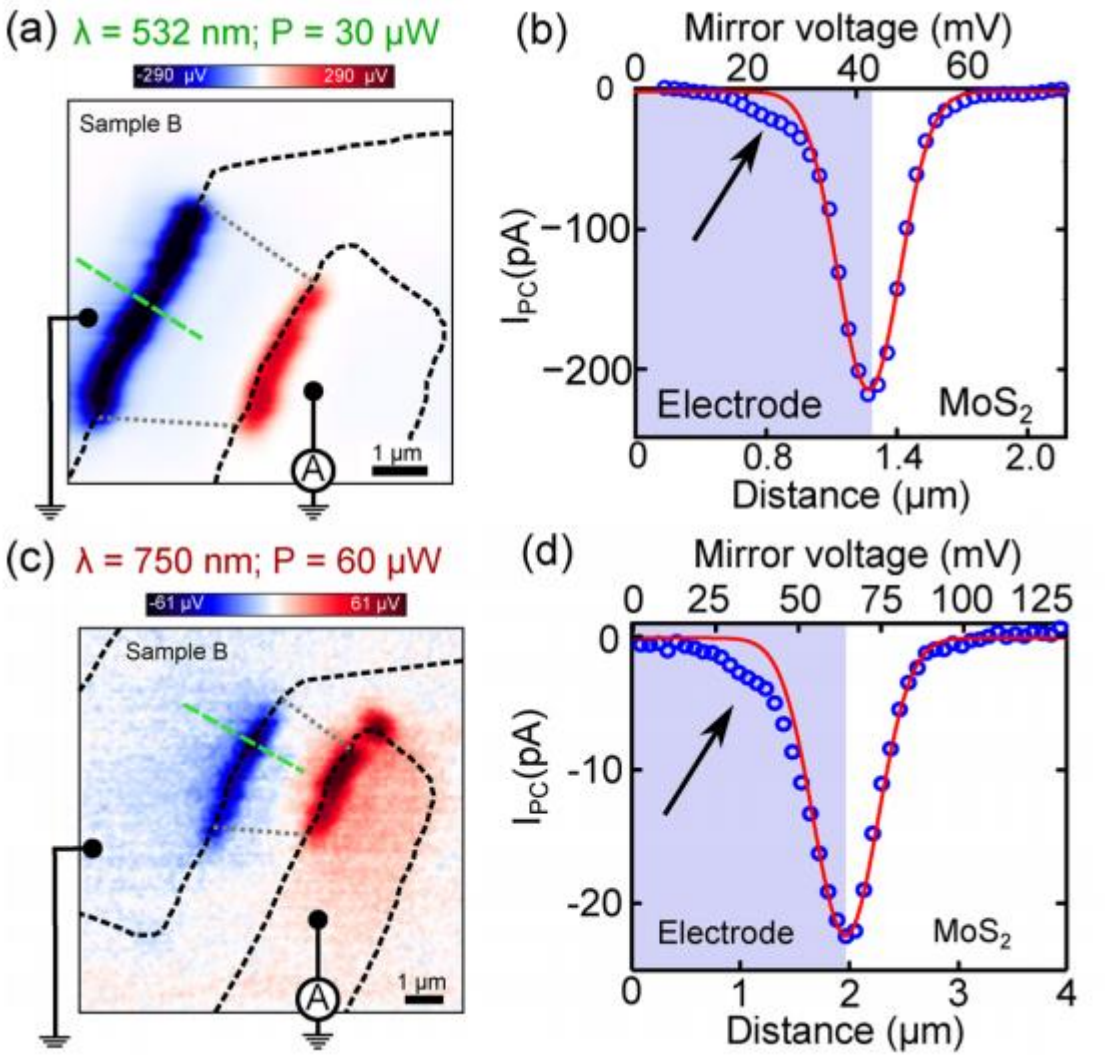

Figure 1.10: Photovoltage map of monolayer MoS_2 using excitation wavelength of (a) 532 nm and (c) 750 nm. (b and d) Photocurrent profile of laser scanning along the green dashed line in (a, c), respectively.

they scanned a laser pointer over the device and measured the current passing through the device. As the laser spot was on the electrode there was a current passing through the device. Since the laser spot was far from the contact edge, several times FWHM of laser spot, this current could not attributed to photogenerated current caused by electron hole

pair generation. They tried two different lase wavelength, one below bandgap and the other above bandgap, the trend was similar for both the laser wavelengths. These results are shown in Fig. 1.10. Parts (a) and (b) corresponds for laser with wavelength of 532 nm which has energies higher than MoS_2 bandgap and parts (c) and (d) corresponds for laser with wavelength of 750 nm which has energy below MoS_2 bandgap. Panels (b) and (d) has depicted the photocurrent corresponding to when the laser pointer maps along the dashed green light in panels (a) and (b), respectively. As noted by an arrow in the current profiles, it is shown that when the laser pointer is still on top of the metal electrode, far from the contact edge, there is a significant amount of current passing through the device. Since this phenomenon is existent in both laser energies, above and below bandgap, it cannot be attributed to electron-pair generation. In the lack of evidence for photogenerated current, authors concluded that photothermoelectric effect is responsible for the observed current through the system. Metal contact absorb the laser light when it is scanned across the metal contact. This absorption of light generates local heating. Since contact metal (Ti/Au) has a different Seebeck coefficient than underlying layer of MoS_2, this local heating translates to a potential difference across the junction. This potential difference consequently leads to a current passing through the device.

In addition to high Seebeck coefficient, low thermal conductivity is also reported for MoS_2 thin films[44,45]. Despite possessing high Seebeck coefficient and low thermal conductivity, bulk MoS2 is predicted to have a low ZT[46] of 0.1 at $700K$ that can be attributed to its poor conductivity[42,47,48]. High pressure is applied to tune interlayer interactions of bulk MoS_2 and its ZT increased to 0.65 over a wide range of temperature

and pressure[49]. In addition, anisotropy in thermal conductance[50] is reported in armchair and zigzag directions and thus providing another degree of freedom to have an optimum design. Taking advantage of higher boundary scattering, hence lower thermal conductance, of one-dimensional (1D) nanoribbons and two-dimensional (2D) sheets in comparison to bulk materials, higher ZT values can be achieved. MoS_2 nanoribbons with widths varying from tens of nanometer to hundreds of nanometer have been synthesized by electrochemical and chemical methods[51,52]. More recently, nanoribbons with uniform widths of just 0.35 nm has been formed in MoS_2 sheets under electron irradiation[53].

Despite the fact that MoS_2 has good properties as a promising thermoelectric material, there is no comprehensive study on thermoelectric properties of 1D MoS_2 nanoribbons and 2D MoS_2 sheets. One of the most important obstacles in achieving devices based on low-dimensional materials is a method leading to a large-scale and uniform growth. There have been lots of effort toward this goal using various chemical vapor deposition (CVD) methods such as sulfurization of metal or metal compounds[54,55] or CVD based on solid precursors (such as MoO_3 or $MoCl_5$)[56,57]. In all these efforts, uniformity of the grown film has been a challenge. More recently, successful uniform monolayer growth of MoS_2 has been reported using MOCVD method[58]. This achievement makes it more important than before to investigate thermoelectric properties of 1D and 2D MoS_2 structures. In this work, thermoelectric properties of pristine 1D monolayer MoS_2 armchair nanoribbons (ACNR) with various widths have been studied. In addition, effect of nanoribbon defects such as edge roughness and Sulfur vacancy on its thermoelectric behavior has been investigated. Moreover, different doping species have been chosen to

replace both Sulfur and Molybdenum in order to achieve n-type and p-type behavior. Thermal current of these doped nanoribbons are also studied. In addition to MoS_2 nanoribbons, 2D sheets of MoS_2 have been studied as well. Effect of sheets orientation, i.e. armchair or zigzag, and also of number of layers has been studied on thermoelectric properties. We have considered monolayer sheets to quad-layer sheets of MoS_2.

1.3 Computational Method

The computational model is based on self-consistent density functional theory (DFT) using non-equilibrium Green's function (NEGF) method[59] implemented in QuantumWise ATK software package. Prior to electronic and phonon calculations, structures have been relaxed to maximum force and stress of $0.05\,eV/\text{Å}$ and $0.05\,eV/\text{Å}^3$, respectively. Generalized gradient approximation (GGA) exchange correlation with a double zeta polarized (DZP) basis set, a mesh cut-off energy of 75 Ha and $10 \times 10 \times 10$ k-point grid is used for relaxation calculations. Large vacuum spacing of at least $20\,\text{Å}$ is added to hinder the effect of periodic images. Landauer-Buttiker[60] formula is used to calculate transport coefficients of the system from Green's function. This formalism is correct in absence of inelastic scattering and phase changing mechanisms. For DFT calculations, Monkhorst-Pack k-grid[61] of $1 \times 1 \times 100$ and DZP basis set with density mesh cut-off of 10 Ha is used for supercell within localized density approximation (LDA).

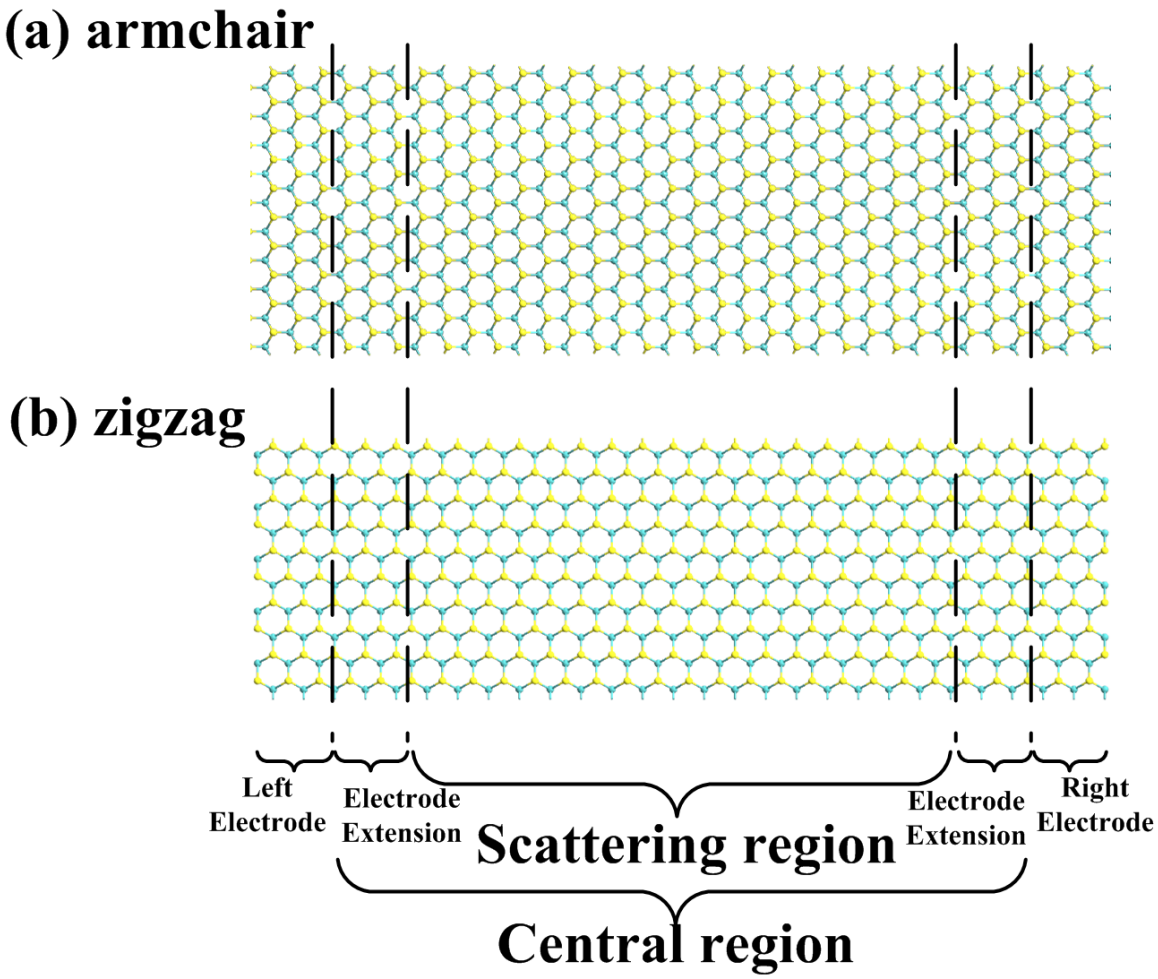

Figure 1.11: Simulated structures in this paper. armchair-oriented and zigzag-oriented MoS_2 are shown in part (a) and (b), respectively. Each device is comprised of three regions: left electrode, central region and right electrode. Central region, itself, contains an extension of electrode regions on both sides and scattering region in the middle. Electrode regions are treated semi-infinitely. Their properties are computed by solving for bulk material. Temperature gradient is biased on electrode regions. Extension of electrode regions in central region, are used to screen out any perturbation introduced in scattering region.

Top view of structures studied in this work is illustrated in Fig. 4. They can be divided into three regions: left, right and central. Left and right regions are called electrodes,

treated with semi-infinite boundary conditions. Their properties can be described by solving for the bulk material. The voltage and temperature bias are applied on electrode regions. Central region includes a repetition of each electrode region in order to screen out perturbations introduced in the scattering regions. In order to have an insight on the thermoelectric properties of intrinsic MoS_2, no perturbation is introduced in the scattering region in calculating ZT. Central region shown in Fig. 4, should be large enough to accommodate both the voltage and temperature drop within itself. The retarded Green's function of channel is calculated as[62]

$$G(E)=\left[(E+i0^{+})I-H-\Sigma_{L}-\Sigma_{R}\right]^{-1} \quad (1)$$

where H is the channel Hamiltonian matrix and $\Sigma_{L(R)}$ is the self-energy due to the semi-infinite left(right) electrode. Electronic transmission per spin through channel region is obtained as

$$T_{e}(E)=tr\left[\Gamma_{L}(E)\cdot G(E)\cdot\Gamma_{R}(E)\cdot G^{+}(E)\right] \quad (2)$$

in which $\Gamma_{L,R}(E)=-2\,\mathrm{Im}(\Sigma_{L,R})$ is broadening function of left and right electrodes and G^{+} is the advanced Green's function.

Carrier transport properties are calculated by a ballistic transport approach under linear response regime. Electrical current I in this regime is given by[60]

$$I=\frac{2q}{h}\int dE\cdot T_{e}(E)\cdot\{f_{L}(E,\mu_{L})-f_{R}(E,\mu_{R})\} \quad (3)$$

in which factor of two counts for spin degeneracy, q is electrical charge of an electron, h is Planck's constant, $T_{e}(E)$ is electronic transmission spectrum, $\mu_{L(R)}$ is chemical

potential of left (right) electrodes and $f_{L(R)}\left(E,\mu_{L(R)}\right)$ is the Fermi distribution of left (right) electrode. Fermi distribution function depends on both chemical potential and temperature. In linear response regime, it is assumed that system is under infinitesimal voltage and temperature bias. As a result, equation (3) will be reduced to

$$I=\frac{2q}{h}\Delta\mu\int dE\cdot T(E)\cdot\frac{\partial f}{\partial\mu}+\frac{2q}{h}\Delta T\int dE\cdot T(E)\cdot\frac{\partial f}{\partial T} \tag{4}$$

where $\Delta\mu$ and ΔT are infinitesimally small. We are interested on pure electrical response of MoS_2 ACNRs to temperature gradient and there is no voltage bias on electrodes therefore $\Delta\mu=0$ and equation (4) will reduce to

$$I=\frac{2q}{h}\Delta T\int dE\cdot T(E)\cdot\frac{\partial f}{\partial T} \tag{5}$$

Electrical conductance (G), Seebeck coefficient (S) and electronic contribution to thermal conductance (κ_e) is calculated by using electronic transmission spectrum as follows

$$G=qL_0 \tag{6}$$

$$S=\frac{L_1}{qTL_0} \tag{7}$$

$$\kappa_e=\frac{1}{T}\left(L_2-\frac{L_1^2}{L_0}\right) \tag{8}$$

where L_n is expressed as

$$L_n=\frac{2}{h}\int dE\cdot T(E)\cdot\left\{-\frac{\partial f(E,\mu)}{\partial E}\right\}\cdot(E-\mu)^n \tag{9}$$

Phonon calculations are performed based on parameterization of Stillinger-Weber potential[63] for MoS_2[45] as implemented in QuantumWise ATK package. Phonon thermal conductance (κ_{ph}) can be calculated as

$$\kappa_{ph} = \lim_{\Delta T \to 0} \frac{\frac{1}{h}\int_0^\infty dE \cdot T_{ph}(E) \cdot E \cdot \{B(E,T_L) - B(E,T_R)\}}{\Delta T} \tag{10}$$

where $T_{ph}(E)$ is phonon transmission spectrum, $B(E,T_{L(R)})$ is Bose-Einstein distribution of the left(right) electrodes, $T_{L(R)}$ is temperature of left(right) electrode and E is energy of transmitted phonon. In linear response regime, temperature bias on electrodes is infinitesimally small. As a result, equation (10) becomes

$$\kappa_{ph} = \frac{1}{h}\int_0^\infty dE \cdot T_{ph}(E) \cdot E \cdot \left(-\frac{\partial B(E,T)}{\partial T}\right) \tag{11}$$

Thermoelectric figure of merit can be readily obtained using these parameters as

$$ZT = \frac{GS^2T}{\kappa_e + \kappa_{ph}} \tag{12}$$

It is worth mentioning that phonon calculations in this paper are performed in absence of any phonon decaying mechanisms. As a result, these calculations set the upper limit for phonon thermal conductance. In real situations, however, there would be a few mechanisms such as scattering centers, crystal imperfectness, surface roughness, etc. which tend to suppress phonon conduction. ZT values calculated in this study are therefore minimum of what actually can be achieved by MoS_2 sheets and nanoribbons.

CHAPTER TWO: THERMOELECTRIC PROPERTIES OF 2D ARMCHAIR AND ZIGZAG MONO- AND FEW-LAYER MOS2 SHEETS

2.1 Electrical Properties of Armchair and Zigzag MoS_2 Sheets

In this chapter, thermoelectric properties of mono-, bi-, tri- and quad-layer MoS_2 in armchair and zigzag directions have been studied for electricity generation. Transmission spectrum characterizes the electrical behavior of the simulated MoS_2 sheets. Electrical factors that affect thermoelectric figure of merit include electrical conductance (G), electronic thermal conductance (κ_e) and Seebeck coefficient (S). These factors can be derived from transmission spectrum as described in the previous section. Transmission spectrums for monolayer and fewlayer MoS_2 in armchair and zigzag orientations are illustrated in Fig. 2.1. Fermi level for intrinsic sheets are located at $E - E_f = 0$.

Further study of Fig. 2.1 indicates that as the number of layers increases from one to four layers, the band gap decreases from $E_g \approx 1.8\,\text{eV}$ to $E_g \approx 1.1\,\text{eV}$ which is in good agreement with previously reported values[64–66]. In addition, the amplitude of transmission spectrum coefficient increases as number of layers increases from one to four, indicating that each layer provides an independent channel to conduct carriers[67]. Furthermore, zigzag orientation is found to have higher transmission coefficients in comparison with armchair and thus is expected to be more conductive than armchair.

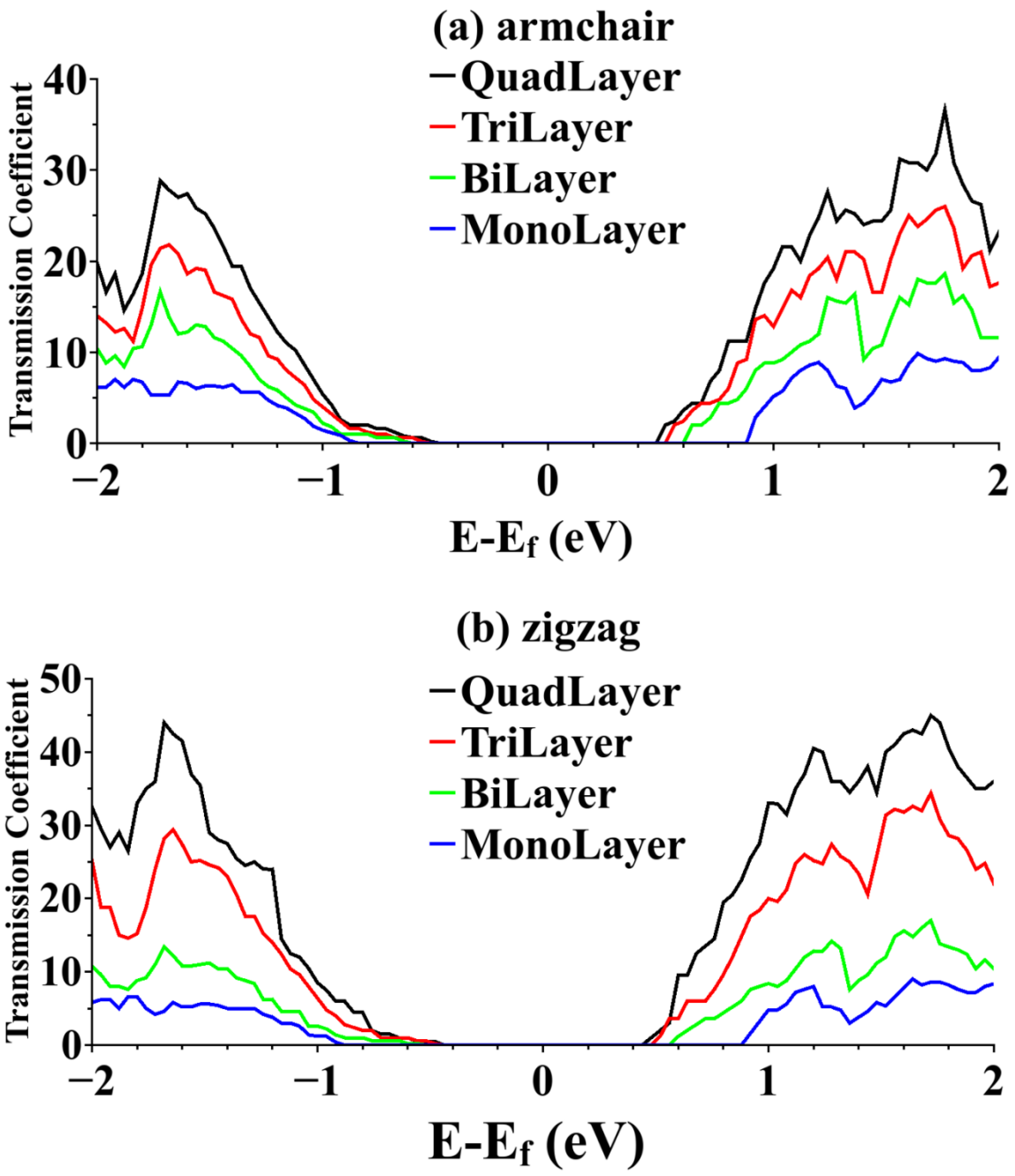

Figure 2.1: Transmission spectra. Transmission spectrum of (a) armchair-oriented and (b) zigzag-oriented for mono-, bi-, tri- and quadlayer MoS_2 calculated based on DFT-NEGF method. Band gap is increasing as number of layers decreases. Transmission coefficients are higher for fewlayer structures, suggesting that each layer provides a conductive channel for carriers.

2.2 Phonon Thermal Conductance of Armchair and Zigzag MoS_2 Sheets

In semiconducting materials, phonon thermal conductance (κ_{ph}) is several times larger than κ_e and outplays the impact of κ_e on thermoelectric figure of merit. κ_{ph} of monolayer and fewlayer for armchair and zigzag orientations vs. temperature are illustrated in Fig. 2.2. As shown in Fig. 2.2, κ_{ph} is almost independent of temperature. It is closely a constant in a wide range of temperatures (from 200K to 500K). In addition, zigzag orientation shows larger κ_{ph} than armchair as was pointed out by Jiang[68] due to the alignment of one vibrational mode in transport direction along zigzag orientation. These results also suggest that κ_{ph} of both zigzag and armchair orientations increases as the number of layer increases. The rate of increase in κ_{ph} is more in zigzag than in armchair orientation. Our results of κ_{ph} for monolayer MoS_2 is in a good agreement with findings by Huang[69].

From factors playing role in thermoelectric figure of merit, G and κ_e follow the profile of transmission spectrum, i.e. as the Fermi level moves into valence or conduction bands, transmission increases, and hence, there are more carriers to be conducted both thermally and electrically. In contrast to G and κ_e, it is typical for semiconductor materials that Seebeck coefficient (S) decreases as Fermi level moves into valence and conduction bands. Therefore G and S are competing with each other and their product in the form of S^2G, known as power factor, reaches its maximum at an optimum position of Fermi energy[69,70].

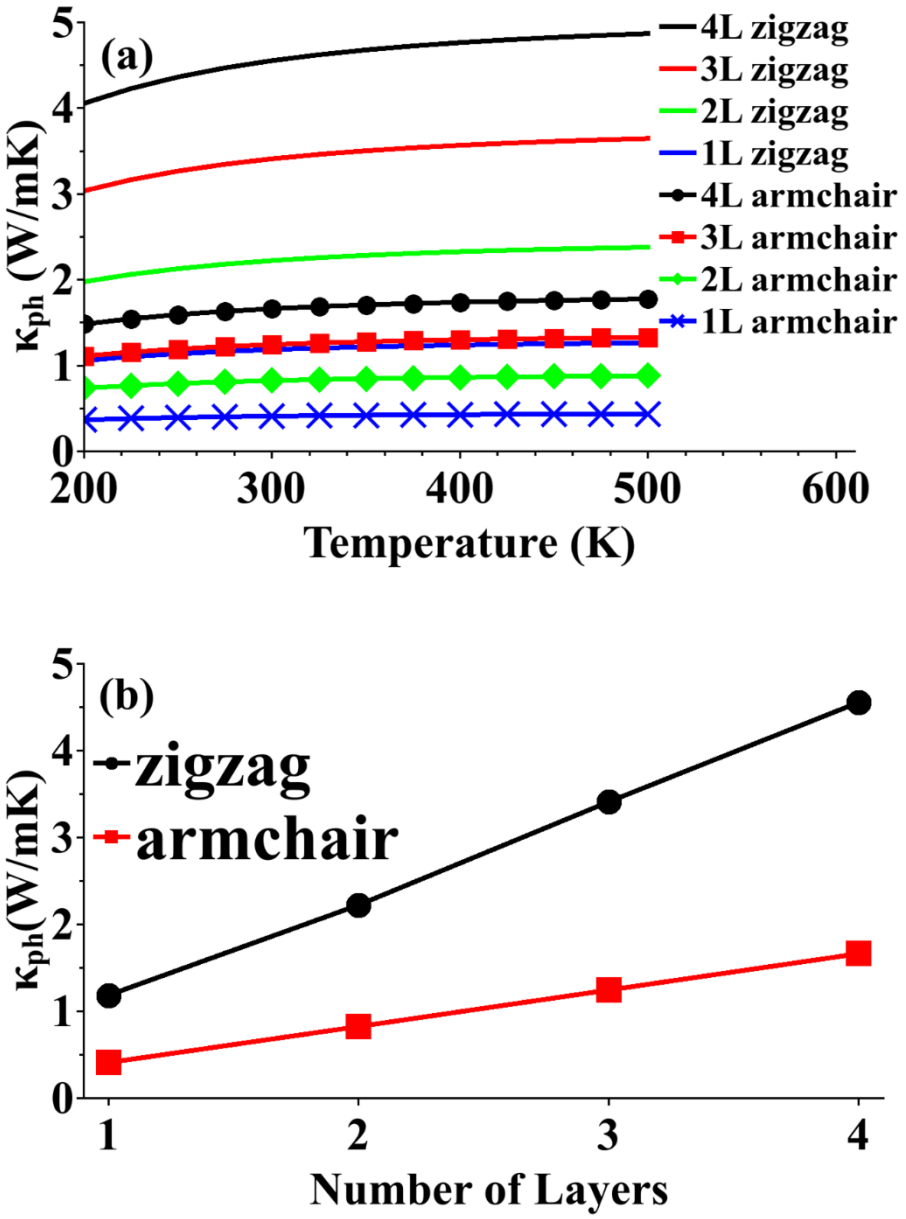

Figure 2.2: Phonon thermal conductance. (a) κ_{ph} vs. temperature for monolayer and fewlayer armchair- and zigzag-oriented MoS_2. (b) κ_{ph}vs. number of layers for armchair- and zigzag-oriented MoS_2 at$T = 300K$. κ_{ph} for zigzag orientation shows higher values and greater rate of increase as number of layers increases from monolayer to quadlayer than those for armchair orientation.

2.3 ZT for Armchair and Zigzag MoS_2 Sheet

ZT values of monolayer and fewlayer MoS_2 in armchair and zigzag orientations vs. Fermi level position at four temperatures are illustrated in Fig. 2.3. There are two main peaks in ZT, separated by a bandgap, corresponding to valence band and conduction band. Valence band maximum (VBM) and conduction band minimum (CBM) are specified in each plot by vertical dashed lines. In this study, thermoelectric figure of merit is referred to as ZT of n-doped or ZT of p-doped as Fermi level is approaching conduction band or valence band, respectively. It is shown in Fig. 2.3 that for all monolayer and fewlayer structures, ZT values of n-doped are higher than those of p-doped.

As temperature increases, amplitude of ZT also increases since ZT is proportional to the temperature. In addition, rising temperature broadens Fermi distribution. This broadening will populate states in energies higher than Fermi level, which were unpopulated in lower temperatures. These newly occupied states contribute to both electrical and thermal conduction. It means that electrical conductance increases in energies which has insignificant contribution to conduction in lower temperatures, resulting in broadening of ZT peaks vs. energy. Further study of Fig. 2.3 shows that profile of ZT broadens as number of layers increases for both armchair and zigzag orientations. This behavior can be attributed to the broadening of transmission spectra of both armchair and zigzag orientations as number of layer increases as illustrated in Fig. 2.1. Despite the increase in transmission coefficients from monolayer to quadlayer, ZT values tend to decrease as number of layers increases. This may be contrary to what is

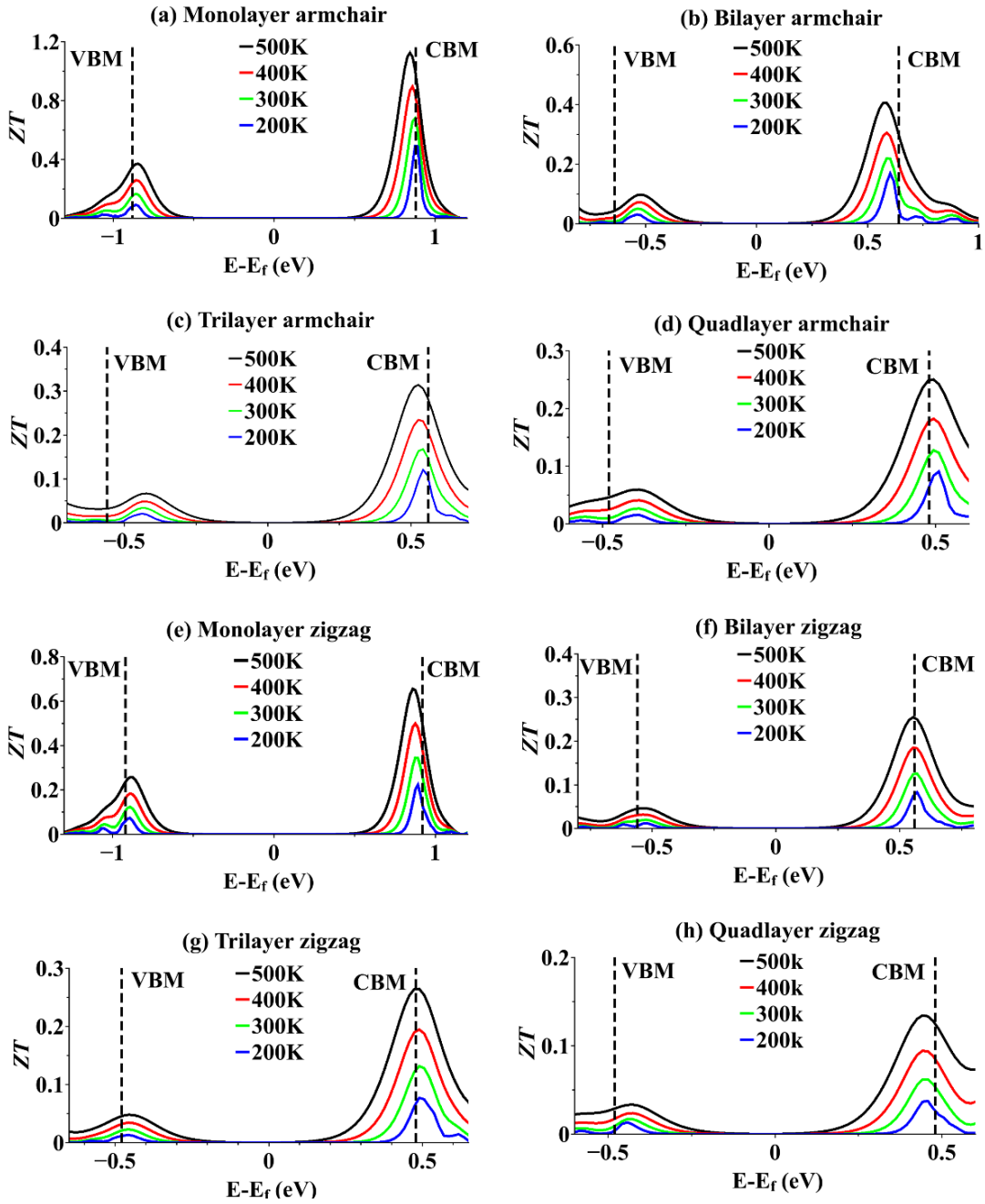

Figure 2.3: Thermoelectric figure of merit. ZT for monolayer and fewlayer armchair- and zigzag-oriented MoS_2 vs. Fermi level position for four temperatures. Conduction band minimum (CBM) and valence band maximum (VBM) are shown by vertical dashed lines in each plot.

expected. One may expect that higher transmission coefficients is equivalent to more conductivity and hence higher ZT value. The reason for this behavior is due to suppression of out-of-plane vibrational mode in monolayer structures. As it can be seen from Fig. 2.3, ZT values undergo a sharp drop as structure changes from monolayer to bilayer for both orientations. This drop in ZT value is less pronounced when structure changes from bilayer to quadlayer. In addition, Fig. 2.3 suggests that ZT value of p-doped

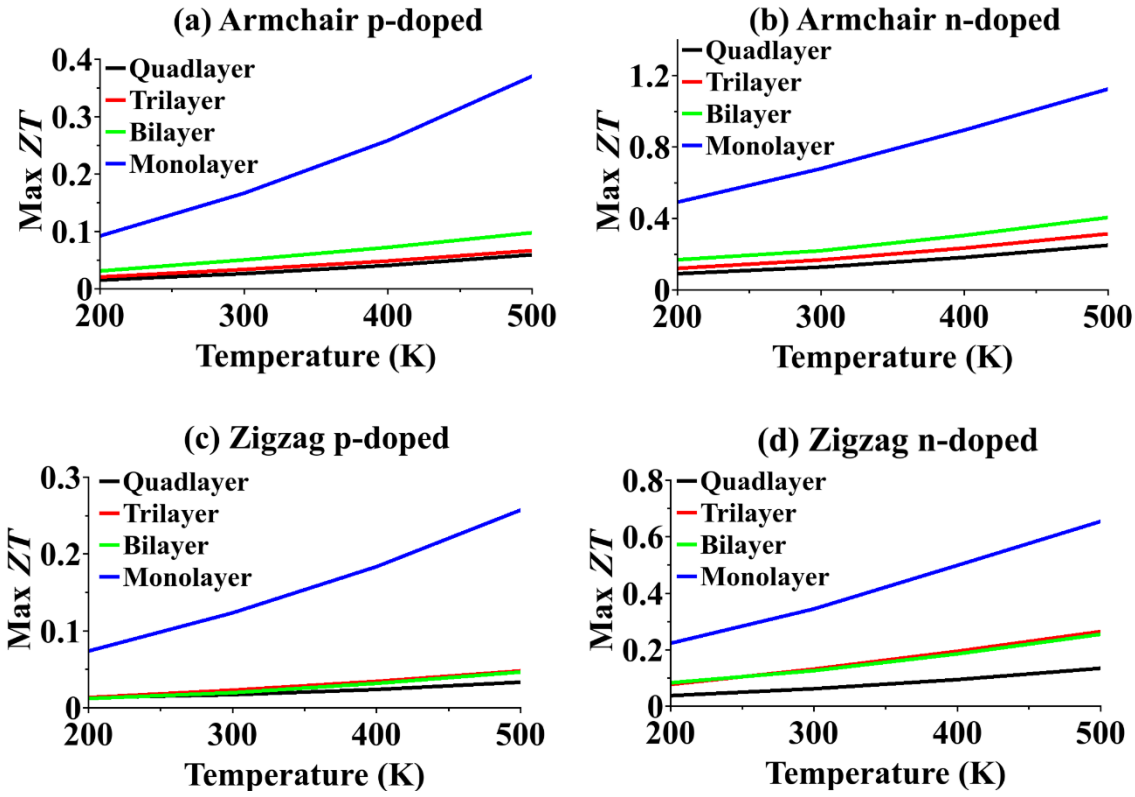

Figure 2.4: Maximum thermoelectric figure of merit. Maximum ZT for p-doped and n-doped monolayer and fewlayer MoS_2 in both armchair and zigzag orientations vs. temperature.

structures are smaller than those of n-doped for both orientations. This characteristic can be attributed to lower growth rate in transmission modes as Fermi level moves into valence band compared to when it moves into conduction band as illustrated in Fig. 2.1.

Peak values of ZT for monolayer and fewlayer armchair and zigzag orientations vs. temperature are shown in Fig. 2.4. As it was expected from equation (12), ZT is approximately linear with temperature. ZT value is monotonously decreasing as number of layer increases. ZT value is larger than unity in n-doped armchair-oriented monolayer at $T = 500K$. This structure has also the highest p-doped ZT value. Therefore, for both n-type and p-type legs in thermocouple, armchair-oriented monolayer MoS_2 is the best choice among all structures studied in this chapter.

2.4 Thermoelectric Current of Armchair/zigzag MoS_2 Sheets vs. Silicon Thin Films

As illustrated in Fig. 2.3, in order to take advantage of the highest ZT value possible, MoS_2 should be doped in order to shift Fermi level to the optimum energy of peak value of ZT profile. Substitutional doping of TMD samples has been observed experimentally under exposure to 80keV electron beam irradiation[71]. Also, a first principal study of effect of this doping approach for transition metal dopants as well as non-metal dopants is reported[72]. In order to examine the thermoelectric current of MoS_2, we have simulated a monolayer MoS_2 in armchair orientation doped with various dopant species. We followed the same substitutional approach for doping our structure. Transition metal atoms (Re, Ru and Ta) are used as the replacing dopants for Molybdenum, and non-transition metal

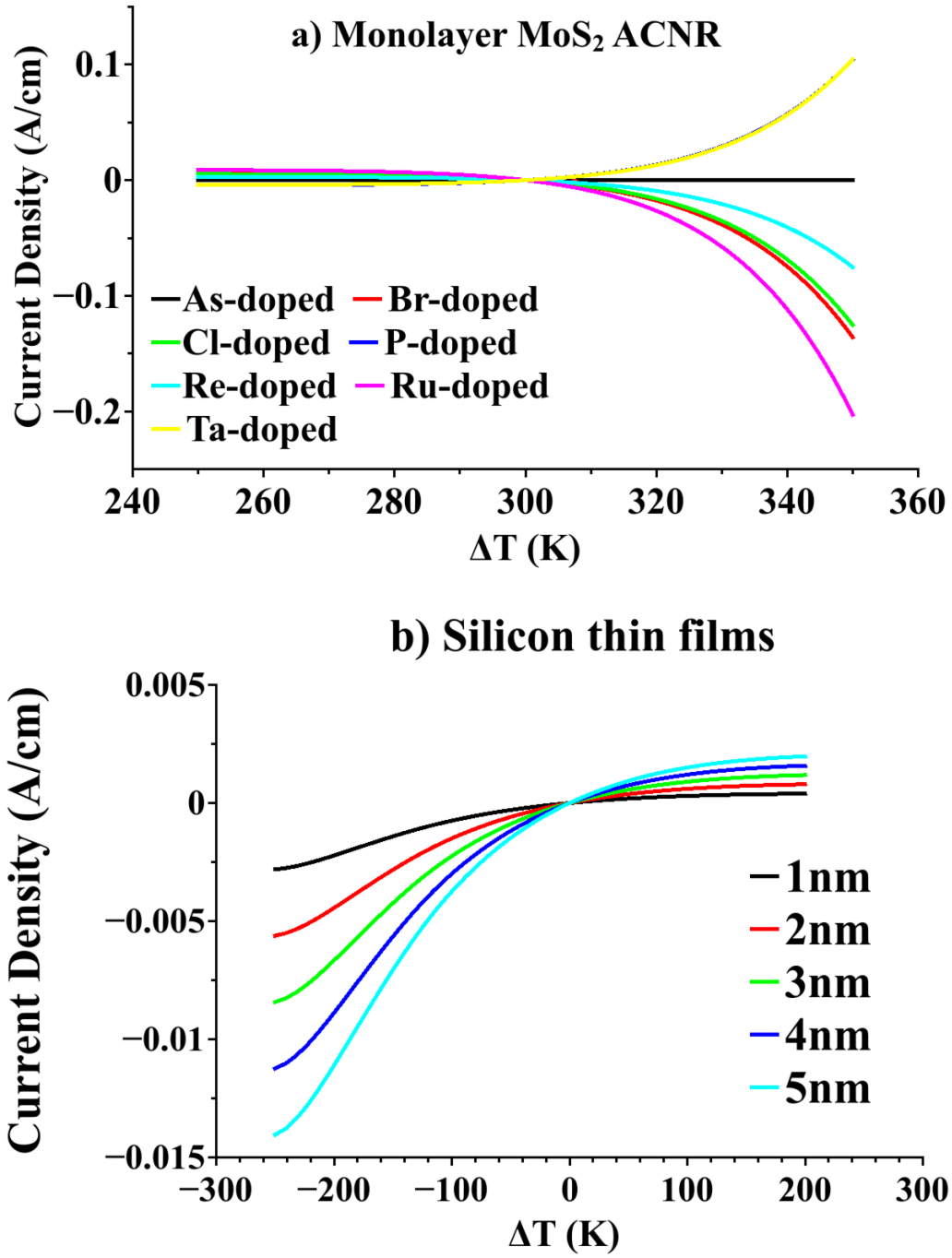

Figure 2.5: (a) Thermoelectric current of armchair-oriented monolayer MoS_2 substitutionally doped with various dopant species versus temperature gradient across it. (b) Thermoelectric current of silicon thin films doped p-type for different film thickness versus temperature gradient across them

atoms (As, Br, Cl and P) are used for Sulphur[73]. In order to screen out the perturbation caused by doping properly, only one dopant atom was inserted in central region of device. A temperature gradient has been set across the nanoribbon by fixing the temperature of right electrode to $T = 300K$ and changing temperature of left electrode from $T = 300K$ to $T = 350K$. Results are shown in Fig. 2.5. Thermoelectric current of monolayer armchair MoS_2 shows strong dependence on the type of dopant atom. While Arsenic does not show any effect on thermoelectric current, P and Ta showed a similar boost to current. For n-type dopant, Ru exhibits the best current boost in comparison with other dopants. It should be noted that doping in MoS_2 monolayer at nanoscale will induce device to device performance variation[74].

These results are compared with TE current of Si thin film doped with acceptor (B) concentration of $N_A = 1\times10^{16} cm^{-3}$ with various film thicknesses (also shown in Fig. 2.5). For Si thin film with film thickness of $t = 5nm$, thermoelectric current density reaches $J \approx 0.001A/cm$ at $\Delta T = 50K$. In comparison, monolayer Ru-doped MoS_2 has thermoelectric current density $J \approx 0.2A/cm$ at $\Delta T = 50K$, more than two orders of magnitude larger. Decreasing thickness of Si film makes them more resistive and thermoelectric current decreases consequently, as shown in Fig. 2.5. Superiority of MoS_2-based thermocouples will be more dramatic if we compare its TE performance with those of thinner Si films, especially $1nm$-thick Si films which is almost the same thickness of monolayer MoS_2.

Thermocouples, as was mentioned in previous section, are made of both p-type and n-type semiconductors. In order to compare the performance of monolayer MoS_2-based and

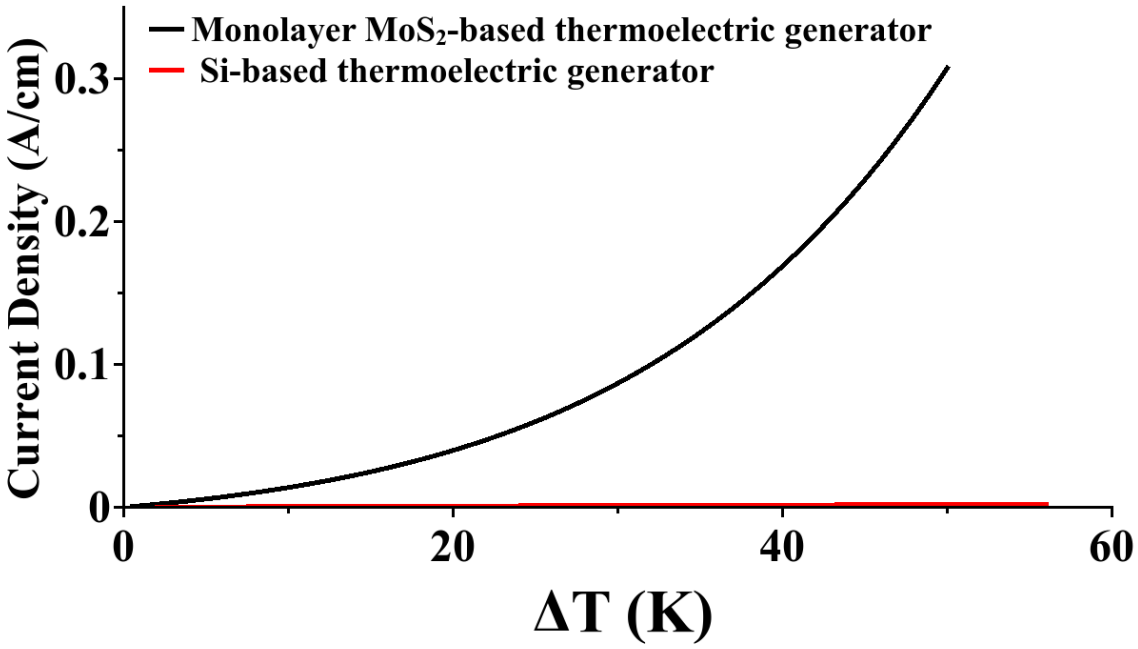

Figure 2.6: Thermoelectric current of thermoelectric generators based on silicon thin film in comparison with that of based on doped monolayer of MoS_2

Si-based thermocouples, TE current of both of these materials is illustrated in Fig. 2.6. For Si-based thermocouples, p-doped (B) and n-doped (As) films with thickness of $t = 5nm$ and with doping concentration of $N_{A,D} = 1\times10^{16} cm^{-3}$ is used. For monolayer MoS_2 thermoelectric conversion, Ru-doped and P-doped are the best n-type and p-type structures, respectively. These two structures are chosen to construct the thermocouple based on monolayer MoS_2. Fig. 9 shows that thermocouples based on monolayer MoS_2 are far more superior to thermocouples based on Si thin films.

2.5 Conclusion

In this part, thermoelectric properties of mono-, bi-, tri- and quad-layer MoS_2 in both armchair and zigzag direction has been studied for electricity generation. It was found that as the number of layer increases from mono-layer to quad-layer, both transmission spectrum and phonon thermal conductance increase. In addition, strong electronic and thermal transport anisotropy is found between zigzag and armchair orientations. Transmission coefficient and phonon thermal conductivity of zigzag orientation is higher than those of armchair with the same number of layers. Their effect on ZT has been studied in this part. Results indicate that by increasing number of layers, ZT value tend to decrease. This behavior was in contrast to the fact that fewlayer MoS_2 is more conductive to monolayer in both directions and can be explained by suppression of out-of-plane vibrational mode in monolayer structure. Among all structures studied, monolayer armchair-oriented MoS_2 is shown to have the highest ZT value as both n-type and p-type semiconducting legs. Also, thermoelectric conversion of silicon thin films thermoelectric generator with the same thickness as MoS_2 armchair mono- and few-layer thermoelectric generator has been studied by using Synopsys TCAD software. The comparison indicated that proposed MoS_2 generator exhibits superior thermoelectric conversion efficiency.

CHAPTER THREE: THERMOELECTRIC PROPERTIES OF MONO-LAYER MOS2 ARMCHAIR NANORIBBONS

3.1 Atomic Structure of MoS_2 Armchair Nanoribbons

Atomic structure of MoS_2 monolayer armchair nanoribbons (ACNRs), as shown in Fig. 3.1, can be considered as monolayer MoS_2 tailored along the armchair direction.

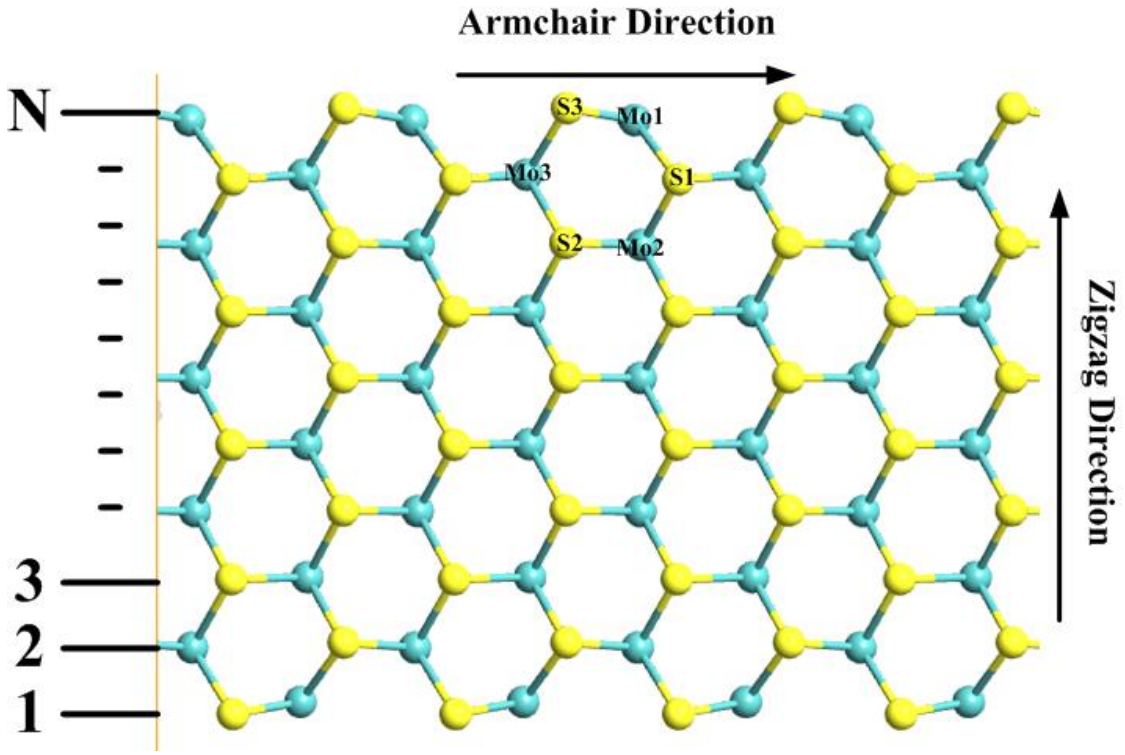

Figure 3.1 Atomic structure of MoS_2 N-ACNR. Atoms at the edge of nanoribbon are labeled to test the degree of reconstruction after relaxation.

ACNRs with various widths can be identified by number of zigzag chains across ACNR width, as illustrated in Fig. 3.1, and are labeled as N-ACNR. In this study, we focus on eight different widths of ACNRs, $N = 3-10$. Width of nanoribbons investigated in this work change from 5.71 Å for 3-ACNR to 16.31 Å for 10-ACNR. Upon relaxation and geometry optimization, atomic structure reconstructs itself. This reconstruction is more pronounced at the edges of nanoribbon than its center. To have a fair idea about the extent of this reconstruction, Fig. 3.1 shows the relaxed structure of 10-ACNR with labeled atoms at the edge of the nanoribbon. It is found that Mo1-S3 bond length decreases from 2.42 Å to 2.34 Å, Mo1-S1 bond length increases from 2.42 Å to 2.46 Å and Mo1-Mo3 bond length decreases from 3.16 Å to 2.97 Å. In addition, bond angle of Mo1-S3-Mo3 decreases from 81.63 to 75.78 degree. Similar reconstruction, not shown here, happens for all ACNRs studied here. This reconstruction is important in determining electronic and transport properties of nanoribbons since electronic states around the Fermi level are mainly edge states[75].

3.2 Electrical Properties of MoS_2 ACNRs

All of monolayer MoS_2 ACNRs that is studied in this work show semiconducting behavior, which is in agreement with previous reports[76,77]. Fig. 3.2 depicts band gap values of these semiconducting MoS_2 ACNRs vs. N, the width identifier. It should be noted that band gap values of ACNRs are much smaller than those of bulk MoS_2 (1.2 eV)[27] and monolayer MoS_2 sheet (1.8 eV)[28]. This behavior cannot be explained by well-

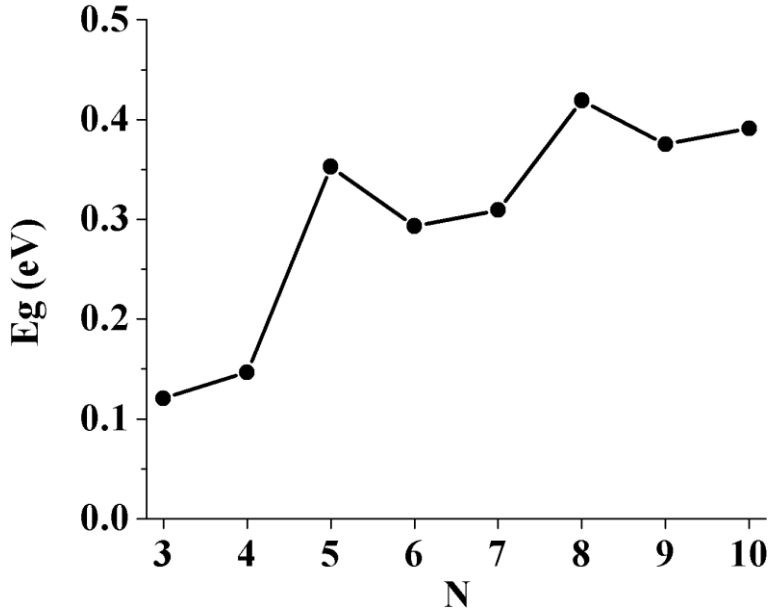

Figure 3.2: Band gap of monolayer MoS_2 ACNR vs. N at $\mu = 0$ Band gap increases as ACNRs widen except for those with $N = 3p-1$ which have larger band gaps than the neighboring ones.

known quantum confinement effects, since those effects tend to increase the band gap. Atoms at the edge of nanoribbons, introduce energy states in the middle of band gap near both valence and conduction bands and therefore narrow the band gap[24]. In addition, Fig. 3.2 illustrates that, band gap values exhibit some sort of oscillation as function of nanoribbon's width. It can be seen that nanoribbons with $N = 3p-1$, p being an integer, have larger band gap than neighboring ones. Same behavior has been reported for Graphene armchair nanoribbons[78] and Silicon armchair nanoribbons[79] and can be generalized as a robust signature of nanoribbons with armchair edges.

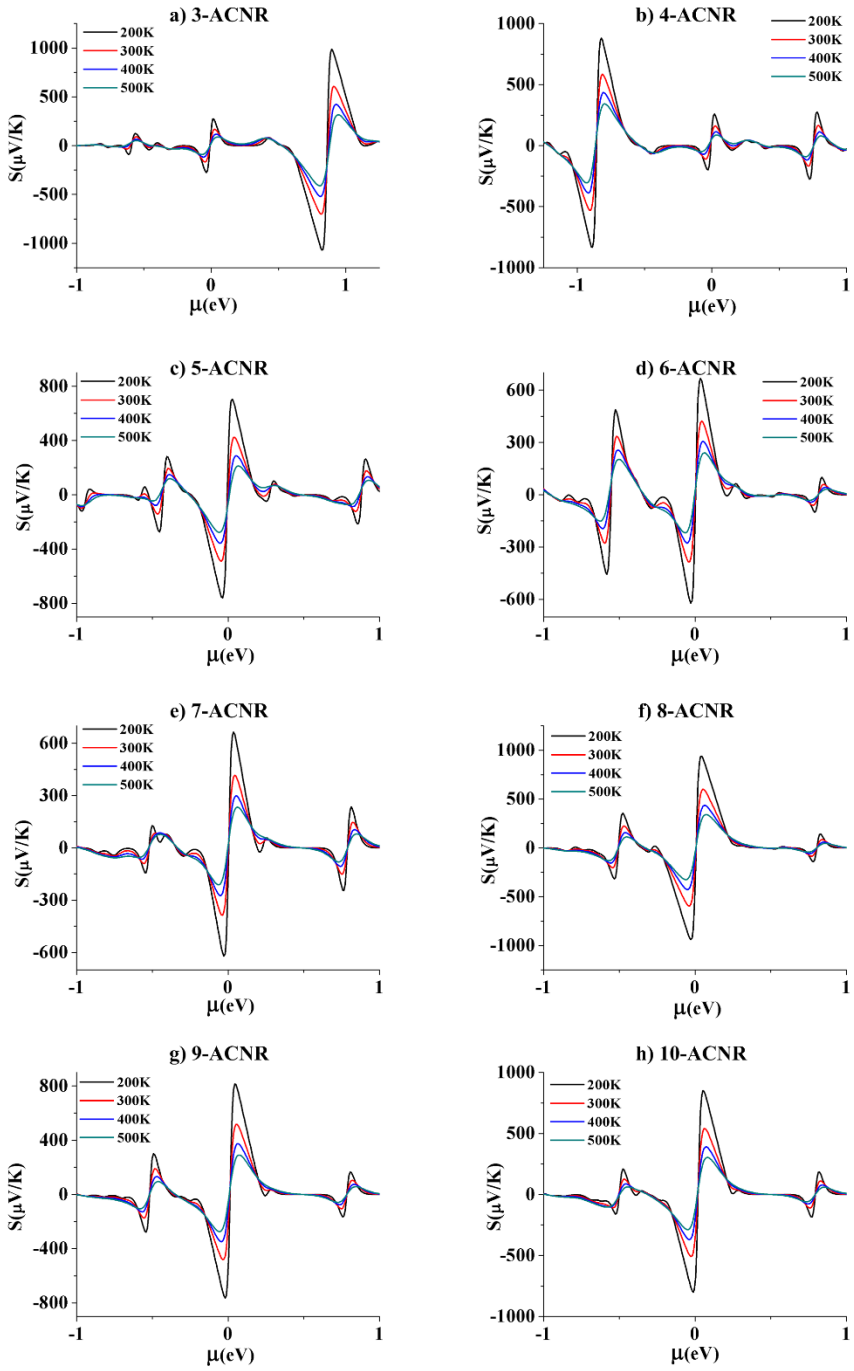

Figure 3.3: Seebeck coefficient for all ACNRs vs. chemical potential for various temperatures. Seebeck coefficient reaches its maximum in gaps of corresponding transmission spectra for each ACNR and its maximum value is proportional to size of band gap and also inversely proportional to temperature.

First, we investigate thermoelectric properties of perfect and defect-free MoS_2 ACNRs. Electronic components of thermoelectric behavior can readily obtain by appropriate integration of transmission function, as discussed in previous section. These integrations involve Fermi distribution function therefore electronic transport coefficients depend on chemical potential and temperature. Chemical potential can shift into positive or negative values by inducing a gate voltage across nanoribbon or by doping it. In rigid band picture, positive and negative chemical potentials correspond to n-type and p-type doping, respectively. Seebeck coefficient as a function of chemical potential (μ) and for different temperatures for all ACNRs investigated in this study is depicted in Fig. 3.3. As it can be seen from equation (7), Seebeck coefficient is inversely proportional to temperature and as temperature increases, peak value of Seebeck coefficient decreases. Seebeck coefficient for ACNRs, shown in Fig. 3.3, follows the same trend. Further study of Fig. 3.3 reveals that Seebeck coefficient of each ACNR comprises of three peaks; one around $\mu = 0$ and one for positive μ and one for negative μ. Peaks of Seebeck coefficient is corresponding to maximum value of transmission-coefficient-weighted average of $(E - \mu)$, see equation (7), which occurs at energies around middle of band gaps of transmission coefficient[80] and absolute value of these peaks increases as band gap increases[81]. Band gap values at $\mu = 0$ is illustrated in Fig. 3.2 and it can be seen that peaks of Seebeck coefficient at $\mu = 0$ follow the same trend as the bandgap values. As nanoribbons get wider, band gap increases, except 5-ACNR and 8-ACNR which have larger band gap than neighboring nanoribbons, and hence Seebeck peaks at $\mu = 0$ also

increases. Transmission spectra of three ACNRs which exhibit distinctive Seebeck coefficient profiles are depicted in Fig. 3.4 in order to further clarify how transmission spectrum affects the Seebeck coefficient. For 3-ACNR and 4-ACNR band gap at $\mu = 0$ is small and in the same order. There is a larger band gap in positive and negative μ for 3-

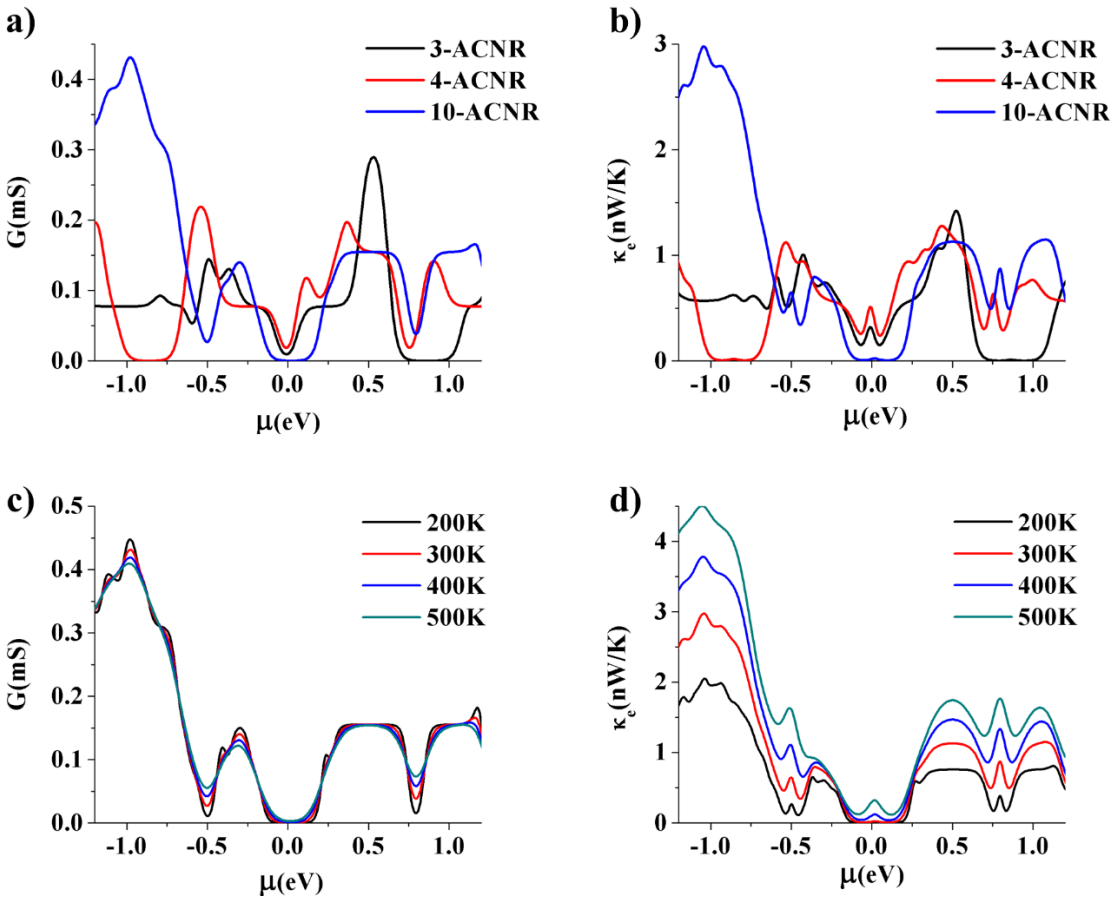

Figure 3.4 Transmission spectra for N-ACNRs with N = 3, 4 and 10. Each transmission spectrum comprised of three band gaps. For 10-ACNR, band gap at $\mu = 0$ is larger than other two. For 3-ACNR and 4-ACNR however, band gap for n-type and p-type (in rigid band picture) is the largest, respectively.

ACNR and 4-ACNR, respectively. It is in agreement with Seebeck coefficient behavior, as for these two nanoribbons peaks at $\mu = 0$ is small in comparison to peak at positive and negative μ for 3-ACNR and 4-ACNR, respectively. Situation for 10-ACNR is opposite and band gap at $\mu = 0$ is larger than other gaps at positive and negative chemical potentials. As a result, Seebeck coefficient reaches its maximum absolute value around

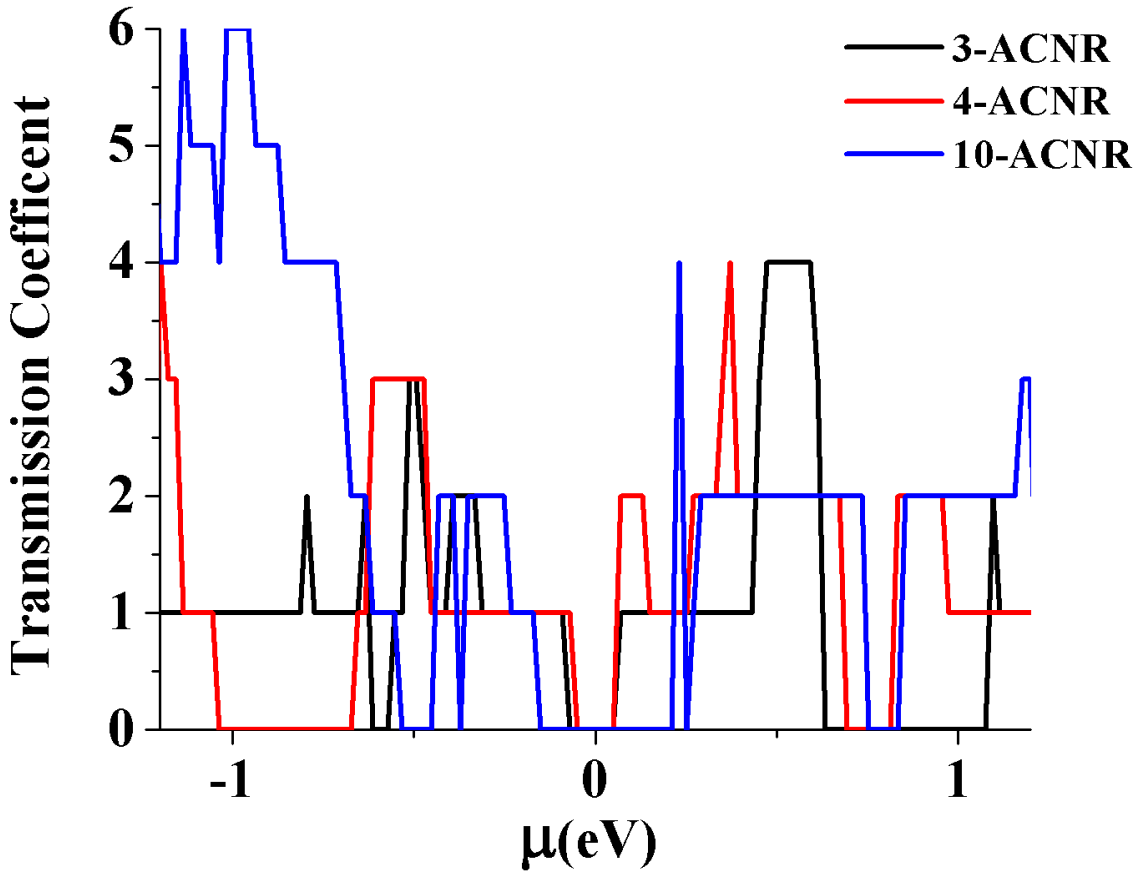

Figure 3.5: Electrical conductance and electronic thermal conductance for N-ACNRs with N = 3, 4 and 10 vs. chemical potential in panels (a) and (b), respectively. Electrical conductance and electronic thermal conductance of 10-ACNR vs. chemical potential for different temperatures are illustrated in (c) and (d), respectively.

$\mu = 0$ for 10-ACNR.

Electrical conductance (G) and electronic thermal conductance (κ_e) are other two electronic transport coefficients that can be obtained from transmission spectra. These two transport coefficients for 3-ACNR, 4-ACNR and 10-ACNR are illustrated in Fig. 3.5. Panels (a) and (b) show electrical conductance and electronic thermal conductance at room temperature for specified nanoribbons, respectively. Profile for both of these transport coefficients follows the same trend as their corresponding transmission spectra vs. chemical potential. As chemical potential moves inside conduction or valence bands, number of channels to conduct carriers both electrically and thermally increases and as chemical potential enters band gaps, both electrical and thermal conductance is supposed to be zero. However, this is not the case for small band gaps in transmission spectra. As depicted for 3-ACNR and 4-ACNR in Fig. 3.5, band gaps at $\mu = 0$ are in order of $5K_BT$ and Fermi function distribution excites some of the transmission channels even when the chemical potential in well inside band gap. As a result, when chemical potential moves into these small band gaps, electrical and thermal conductance decreases but does not drop to zero. Similar behavior can be seen for band gaps in positive and negative chemical potentials for 10-ACNR. However, as shown in Fig. 3.4, 10-ACNR has a comparatively larger band gap at $\mu = 0$. Moreover, 3-ACNR and 4-ACNR have band gaps in the same order in positive and negative values of μ, respectively. As chemical potential moves inside these band gaps, they are in order of $15K_BT$, electrical and thermal conductance drop to zero. Panels (c) and (d) of Fig. 3.5 illustrates electrical and

thermal conductance of 10-ACNR vs. chemical potential for different temperatures. It can be seen from panel (c) that for larger band gap at $\mu = 0$, electrical conductance does not change very much as temperature increases while in smaller band gaps in positive and negative chemical potentials as temperature increases, electrical conductance drop less. This behavior is due to broadening of Fermi function distribution. For higher temperatures, Fermi distribution is broader and excites more states in neighboring bands than in lower temperature. This effect is more pronounced in smaller gaps compared to larger band gaps. Electronic thermal conductance of 10-ACNR for different temperatures is illustrated in panel (d) of Fig. 3.5. In higher temperatures more carriers will be conducted thermally and electronic thermal conductance increases.

3.3 Phonon Thermal Conductance of MoS_2 ACNRs

Phonon thermal conductance $\left(\kappa_{ph}\right)$ has been obtained by parametrization of Stillinger-Weber potential for MoS_2. In contrary to electronic thermal conductance, phonon thermal conductance is not affected by changing chemical potential and is constant as μ changes. Phonon thermal conductance increases as temperature increases, as shown in panel (a) of Fig. 3.6 (not shown for all ACNRs). In addition, it can be seen that rate at which phonon thermal conductance increases vs. temperature is higher for wider nanoribbons than for narrower nanoribbons. Moreover, phonon thermal conductance at room temperature for all ACNRs is illustrated in panel (b) of Fig. 3.6. As nanoribbons get wider, phonon thermal conductance increases. In narrower nanoribbons, there are less channels to

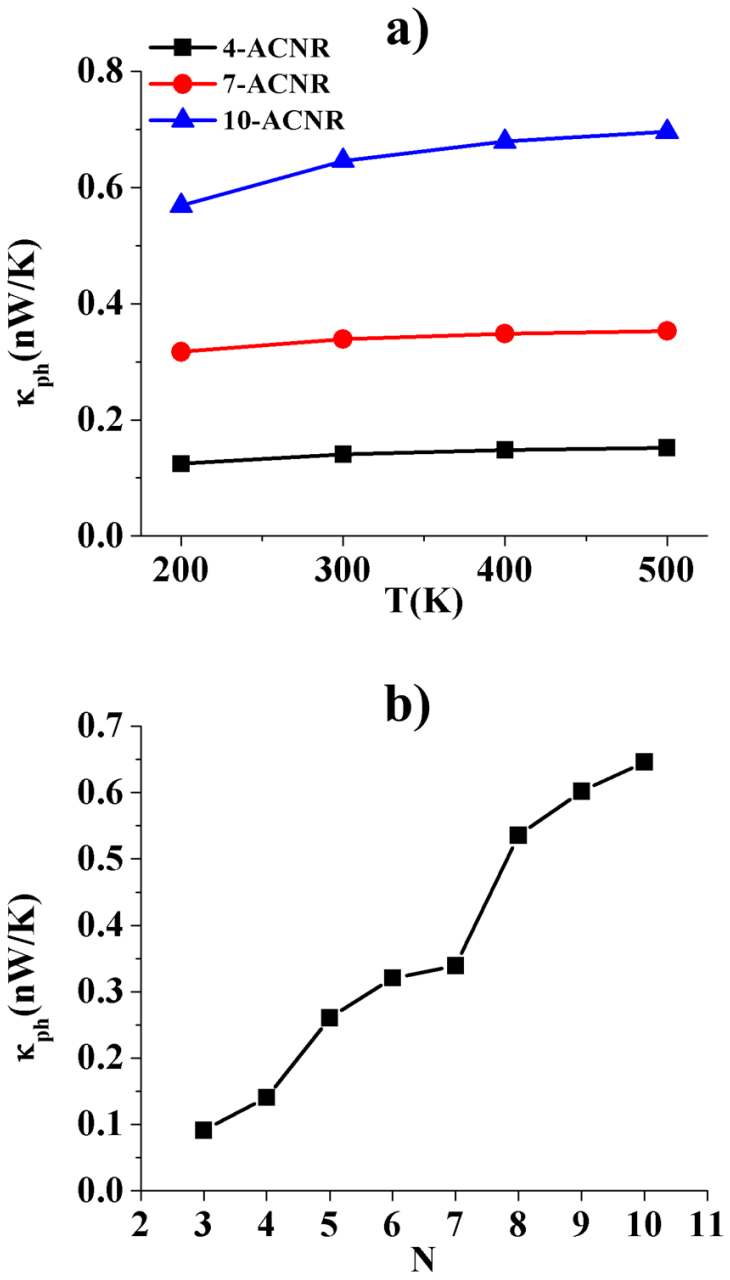

Figure 3.6 (a) Phonon thermal conductance for N-ACNR with N=4, 7 and 10 vs. temperature. Rate of increase in phonon thermal conductance vs. temperature is more for wider ACNRs compared to narrower ones. (b) Phonon thermal conductance at room temperature for all ACNRs.

conduct heat by phonons and effect of edge phonon scattering is more profound

compared to wider nanoribbons. As nanoribbons widen, there are more available channels for phonons to conduct heat and overall effect of boundaries decreases[82].

3.4 ZT for MoS_2 ACNRs

Now we have all parameters and thermoelectric figure of merit, $ZT = \frac{GS^2}{\kappa_e + \kappa_{ph}} T$, can readily be obtained. ZT values of all MoS_2 ACNRs as a function of chemical potential and for various temperatures have been illustrated in Fig. 3.7. Seebeck coefficient, as can be seen from Fig. 3.3, reaches its maximum within energies about $K_B T$ of middle of each band gap and as chemical potential approaches conduction or valence subbands, it rapidly drops. In contrary, electrical conductance increases when chemical potential moves from energy band gaps and approaches conduction or valence subbands. Therefore, ZT peaks are located at some optimized energy at which these two competing factors in form of GS^2 reaches its maximum. It is expected that ZT increases approximately linearly as temperature increases[83]. However, further study of Fig. 3.7 reveals that it is not always the case in our results. Each ZT profile, similar to Seebeck coefficient profiles, comprises of three major peaks; one about $\mu = 0$ and two for positive and negative values of chemical potential. These peaks are located about band gaps in corresponding transmission spectra. It can be seen that ZT peaks that are located in small band gaps, i.e. band gap for n-type 3-ACNR or for p-type 4-ACNR, decreases as temperature increases. This behavior can be explained by temperature dependence of electrical conductance at these small band gaps. Seebeck coefficient is inversely proportional to temperature for all its peaks. As a result, the discrepancy of ZT peaks at smaller band gaps should be

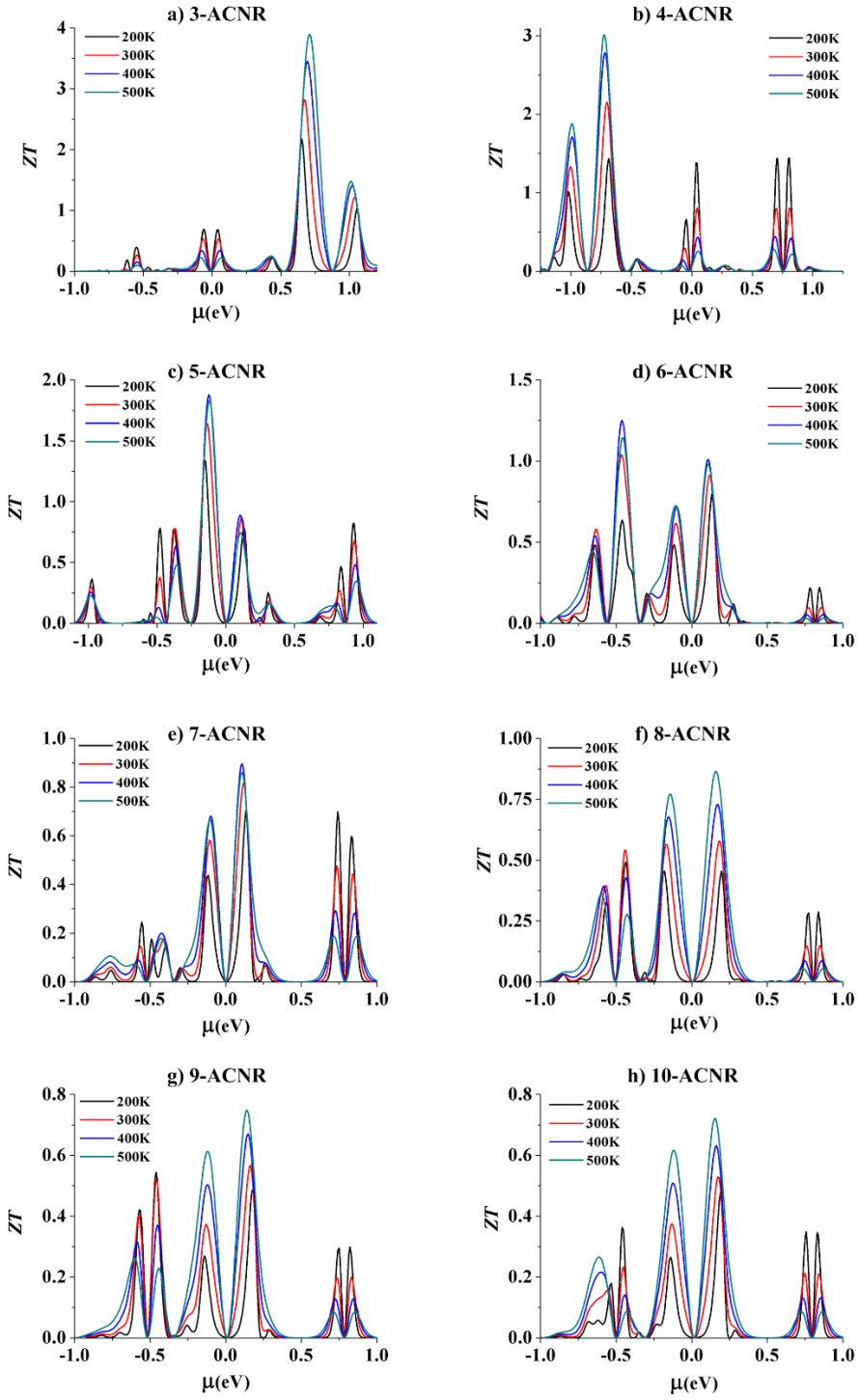

Figure 3.7: ZT of N-ACNR for N = 3 to 10 vs. chemical potential for different temperatures in (a) through (h)

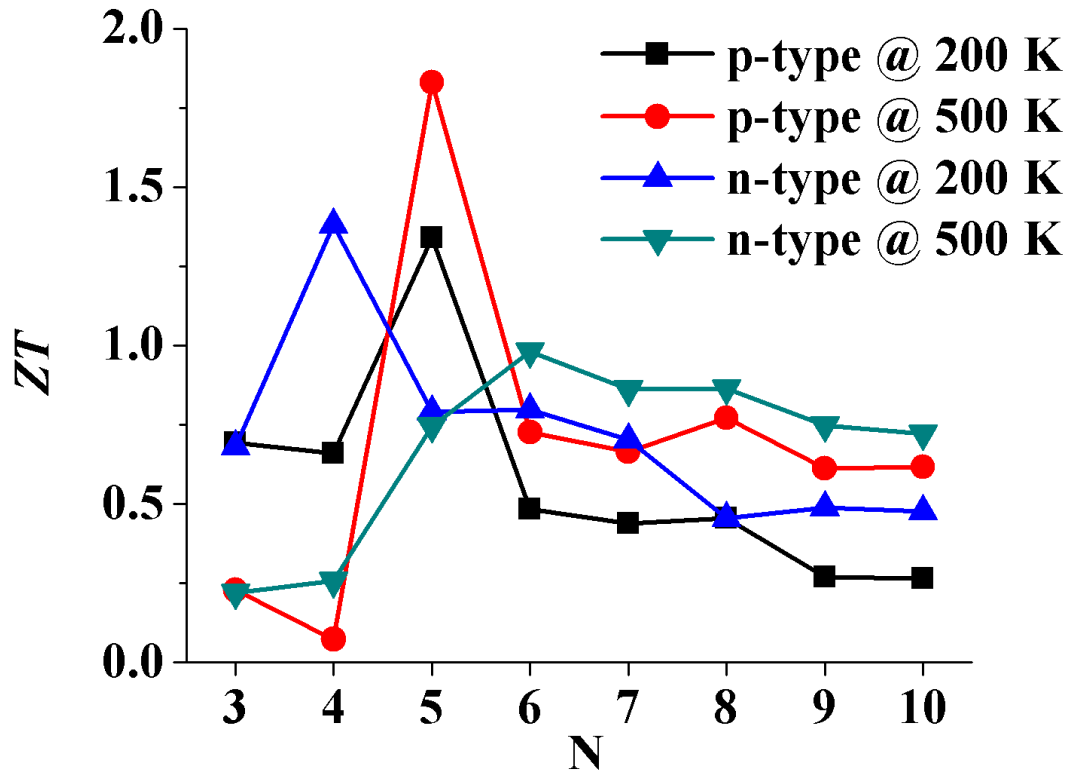

Figure 3.8: Maximum value of p-type and n-type ZT peaks for all ACNRs at T = 200 K and T = 500 K.

affected by electrical conductance. It has been explained earlier that as chemical potential moves inside small band gaps, drop in electrical conductance is less as temperature increases (see Fig. 3.5). This behavior was explained by broadening of Fermi distribution function. It can be noted from Fig. 3.7 that for ZT peaks located at energies corresponding to larger band gaps, maximum value increases vs. temperature. It is specified that band gap at $\mu = 0$ increases as nanoribbons widen, except for 5-ACNR and 8-ACNR for which band gap is larger than their neighboring ones. In order to clarify this

behavior, Maximum value of ZT located around $\mu = 0$ for both p-type and n-type (in rigid band picture) MoS_2 ACNRs is depicted in Fig. 3.8 for two temperatures. It has been shown that for 3-ACNR and 4-ACNR both ZT values of p-type and n-type at $T = 200K$ is higher than those at $T = 500K$ and as N increases and therefore bandgap increases, ZT values at $T = 500K$ becomes higher than those at $T = 200K$. Our calculation has shown that ZT values larger than unity can be achieved by MoS_2 ACNRs. For n-type nanoribbon, ZT value of 2.82 at room temperature and $\mu = 0.67eV$ can be achieved in 3-ACNR. For p-type, nanoribbon, ZT value of 2.16 at room temperature and $\mu = -0.7eV$ can be achieved in 4-ACNR. In higher temperatures ZT values in order of 3 and 4 can be obtained. These ZT values are far superior to those of bulk or monolayer and multi-layer sheets of MoS_2 (refs. 29, 32 and 34).

3.5 Impact of Defects on Thermoelectric Behavior of MoS_2 ACNRs

In addition to perfect MoS_2 ACNRs, effect of two types of defect on thermoelectric properties of MoS_2 nanoribbons is also studied; Sulfur vacancy and edge roughness. For both of these defects 10-ACNR has been adopted as the framework. Sulfur vacancy is formed by removing a Sulfur atom from the center of the nanoribbon and edge roughness has been formed by deliberately degrading the perfect structure of nanoribbon at its edge (illustrated in inset of panel (a) of Fig. 3.9). Both of these defect-induced structures have been relaxed using the same parameters of ACNRs relaxation. Effect of these defects on transport coefficients at room temperature shown in Fig. 3.9. Panel (a) shows

transmission spectra of defect-free 10-ACNR as well as of those with Sulfur vacancy and edge-roughness. Due to translational symmetry breakage in defect-induced ACNRs, transmission spectra have been deviated from stepwise profile to more smooth ones. Moreover, it can be seen that both of defects has decreased transmission coefficients of nanoribbons which leads to drop in electrical conductance and electronic thermal

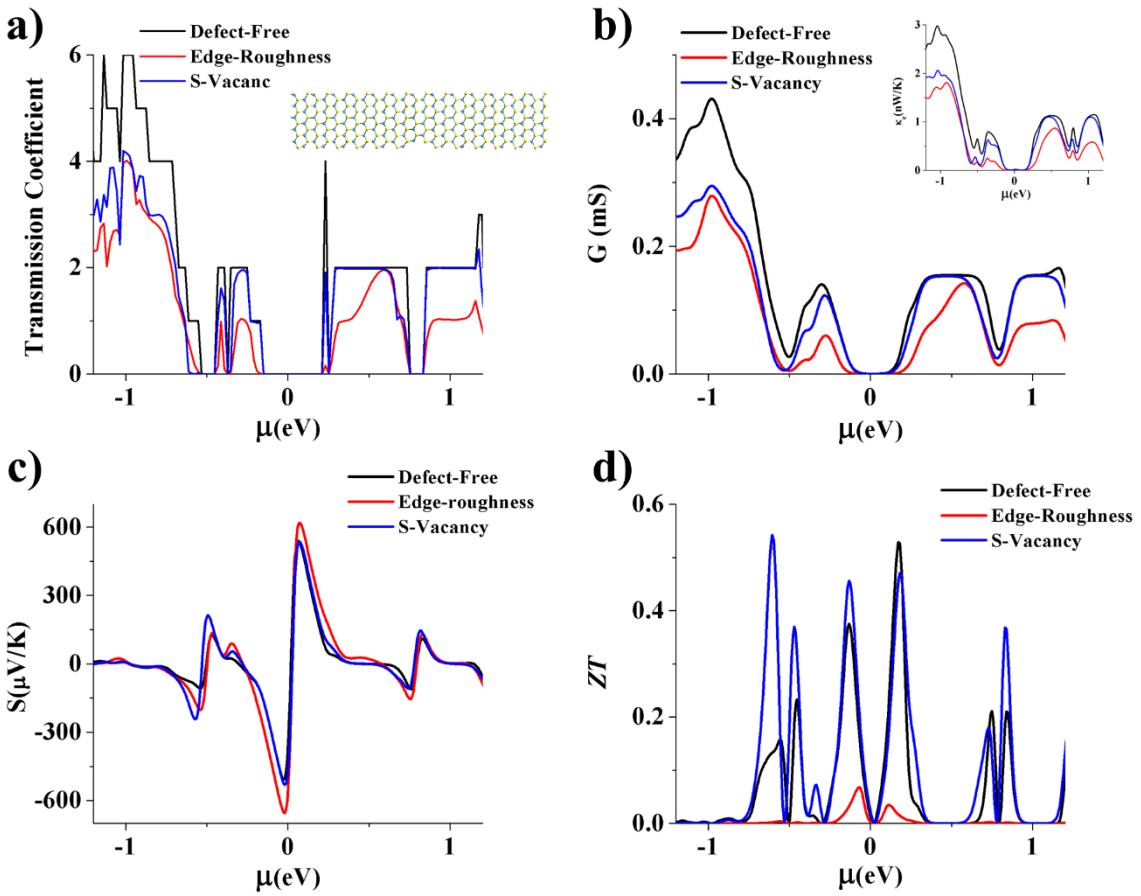

Figure 3.9: Effect of Sulfur vacancy and edge roughness has been studied on thermoelectric properties of 10-ACNR and compared with those of the perfect nanoribbon; (a) Transmission spectra, inset shows atomic structure of 10-ACNR with edge roughness, (b) Electrical conductance, inset depicts electronic thermal conductance, (c) Seebeck coefficient and (d) ZT.

conductance of nanoribbons as is depicted in panel (b) and its inset. It can be seen that carrier conductance, both thermally and electrically, has been degraded more by edge roughness compared to Sulfur vacancy. Further study of transmission spectra reveals that edge roughness expectedly affects edge conduction, which corresponds to higher valence and lower conduction subbands, more tremendously than Sulfur vacancy. In contrast to carrier conductance, change in Seebeck coefficient of ACNR with Sulfur vacancy is negligible compared to perfect ACNR and for nanoribbon with edge roughness Seebeck coefficient increases. However, for lower valence sub-band, Seebeck coefficient has been increased in comparison to perfect ACNR. This can be explained by the fact that Seebeck coefficient is proportional to transmission-weighted average of $(E-\mu)$. At a given temperature, in order to have a higher Seebeck coefficient, transport of carriers with lower $(E-\mu)$ should be suppressed. By inducing edge roughness, sharp and step-wise increase of transmission coefficient at valence and conduction subband edges has been smoothed and transport of those carriers has been suppressed compared to carriers with higher energies. This situation has not happened in case of ACNRs with Sulfur vacancy and edge of valence and conduction subbands have the same step-wise shape as in perfect ACNR. In addition to electrical transport coefficients, defects have affected phonon thermal conductance as well. In the case of perfect ACNR $\kappa_{ph} = 0.65\,\text{nW/K}$, sulfur vacancy reduces it to 0.51 nW/K and edge roughness reduced it further to 0.36 nW/K. It can be noted form panel (d) of Fig. 3.9 that drop in electrical conductance and increase in Seebeck coefficient in ACNRs with rough edge has been marginalized by drop in electrical conductance and ZT has been reduced tremendously compared to perfect

ACNR. However, Sulfur vacancy which has not degraded electrical conductance as much as edge roughness, improved ZT in some subbands. ZT values for p-type ACNR has been boosted by Sulfur vacancy compared to perfect ACNR.

In order to examine thermoelectric sensitivity of monolayer MoS_2 ACNRs, $\frac{I}{\Delta T}$ from equation (5) been calculated and results are depicted in panels (a) and (b) of Fig. 3.10. It can be noted from equation (5) that thermoelectric sensitivity of nanoribbons depends on two factors; 1) transmission coefficient and 2) rate of change in Fermi distribution function with respect to temperature. Fermi distribution flattens to one and zero as it goes to energies in order of several $K_B T$ lower and higher than chemical potential, respectively. As a result, transmission channels at lower energies of conduction band and higher energies of valence band play the dominant role in determining thermoelectric sensitivity of monolayer MoS_2 ACNRs. In addition, as temperature increases Fermi distribution broadens and more transport channels involve in thermoelectric conversion and consequently sensitivity increases. Moreover, it is expected that as band gap decreases, assuming equal transmission coefficients, more transport channels are covered by Fermi distribution and hence higher thermoelectric sensitivity will be achieved. Panels (a) and (b) of Fig. 3.10 illustrate that some ACNRs show n-type behavior while others show p-type behavior. It can be explained by their transmission spectra profile. Small band gap of 3-ACNR and high transmission coefficient of 10-ACNR made these two nanoribbons the most thermoelectrically sensitive among p-type ACNRs. Sensitivity of 5-ACNR, depicted in panel (b) of Fig. 3.10, which is showing n-type behavior, is one

order of magnitude larger than the best p-type ACNR.

In addition, various transition metal elements have been used to study of doping on thermoelectric behavior of ACNR. Zirconium (Zr), Niobium (Nb), Hafnium (Hf), Technetium (Tc) and Ruthenium (Ru) have been chosen to replace Molybdenum (Mo) in 10-ACNR. After replacing Mo with each of these elements, structure has been relaxed to minimize force and stress. Doped ACNRs are supposed to benefit a higher thermoelectric sensitivity by shifting the Fermi level toward valence or conduction band edges. Although the fermi level is shifted but introducing these dopants to lattice of MoS_2 ACNRs has distorted lattice structure which leads to drop in transmission coefficient. Drop in transmission coefficients has a stronger impact than shift in Fermi level and, as it is shown in panel (c) of Fig. 3.10, thermoelectric sensitivity of doped 10-ACNR is less than undoped 10-ACNR. In addition to doped 10-ACNRs, effect of Sulfur vacancy does not show any effect on sensitivity.

3.6 Conclusion

In this part, we have studied thermoelectric properties of monolayer MoS_2 armchair nanoribbons. These nanoribbons are identified by number of zigzag chains across the ribbon denoted as N-ACNR. The effect of the size of nanoribbons on their thermoelectric behavior by considering N = 3-10 has been studied. Transmission spectra of ACNRs are comprised of edge states for both electrons and holes. This leads to existence of three gaps in transmission spectra. AS the width of the nanoribbon increases, the Seebeck

coefficient and ZT at the center gap also increases. Phonon thermal conductance decreases by narrowing down the nanoribbons due to an increased impact of phonon edge scattering on overall phonon thermal conductance. As a result, the maximum ZT values that can be achieved by narrow ACNRs are higher than the wider ones. The effect of sulfur vacancy and edge roughness on thermoelectric properties is also studied. It is found that, although edge roughness will decrease phonon thermal conductance, the degradation in electrical conductance leads to a tremendous drop in *ZT*. In contrast to edge roughness, a sulfur vacancy decreases phonon thermal conductance without

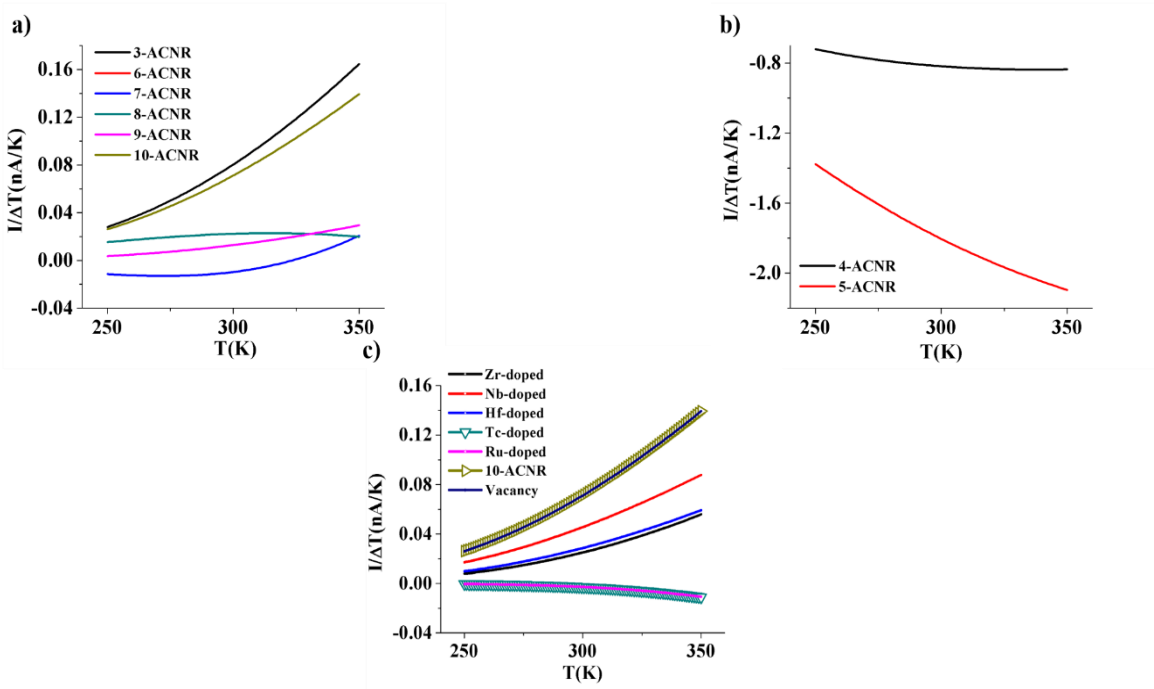

Figure 3.10: Thermoelectric sensitivity of all ACNRs vs. temperature are illustrated in (a) and (b). Effect of doping on thermoelectric sensitivity of 10-ACNR has been studied and compared to that of with a Sulfur vacancy and also to the perfect 10-ACNR.

degrading electrical conductance as much as edge roughness, leading to an increased *ZT* value at some energies. It has been shown that *ZT* value as high as $ZT = 4$ in 3-ACNR for n-type material and $ZT = 3$ in 4-ACNR for p-type material at $T = 500K$ can be achieved. Possibility of gaining high *ZT* values for both n-type and p-type material makes monolayer MoS_2 ACNRs a promising candidate in future thermoelectric generators.

CHAPTER FOUR: GATE EFFECT ON THERMOELECTRIC PROPERTIES OF MOS2 ARMCHAIR NANORIBBONS

4.1 Introduction and Motivation

Thermoelectric properties of MoS_2 monolayer and multilayer infinite sheets in both armchair and zigzag directions have been studied in chapter 2. It has been shown that thermoelectric figure of merit of larger than one can be achieved in monolayer MoS_2 armchair sheet. Although this large thermoelectric figure of merit can be achieved, but a large fermi level shift is required. A fermi level shift of about 1eV is required to take advantage of the excellent thermoelectric performance of monolayer MoS_2 armchair sheets. The other disadvantage of MoS_2 sheets was that they have high thermoelectric figure of merit for n-type behavior only. Their thermoelectric figure of merit for p-type behavior was lower than conventional thermoelectric materials.

In chapter 3, thermoelectric properties of MoS_2 armchair nanoribbons have been studied and both of the disadvantages of MoS_2 sheets have been addressed. By tailoring MoS_2 sheets and forming MoS_2 nanoribbons, some edge electronic states have risen in the band gap and cause the band gap to shrink significantly. As a result, smaller amount of fermi level shift is required to achieve the peak values of thermoelectric figure of merit. Also anisotropy between p-type and n-type thermoelectric behavior has been taken care of and equally high thermoelectric figure of merit can be achieved for p-type as well.

But to achieve these high thermoelectric properties, slight fermi level shift and doping is required. Doping can be very challenging when dealing with nanoribbons of monolayer MoS_2 of just couple of nanometers in width. It can have its downsides as well by increasing the tension in lattice structure and therefore increasing the scattering and degrading the conductance. An alternate approach to doping would be attaching molecules to the active region and electrostatically dope the channel. But this approach is not practical in large-scale view and also suffers from sample-to-sample variance. Another alternate approach to shift the fermi level toward energies with high thermoelectric figure of merit. It is a known phenomenon that by applying a gate voltage on a semiconductor and populating excess free carriers fermi level shifts toward conduction or valence band edges, depending on the polarity of the applied gate voltage. Shifting the fermi level toward band edges will increase electron or hole population depending on what band edge the fermi level is approaching. This increase in population of electron/hole causes the electrical conductance to increase. Electrical conductance and Seebeck coefficient are strongly dependent and as electrical conductance increases, Seebeck coefficient decreases. As a result, there is a competing effect on thermoelectric figure of merit from electrical conductance and Seebeck coefficient. In following sections, we first study the effect of gate voltage on electrical conductance and then we study the impact of gate voltage on Seebeck coefficient profile. In the last section of this chapter, we study these counter influential effects on thermoelectric figure of merit of monolayer MoS_2 armchair nanoribbons.

4.2 Gate Impact on Electrical Conductance of MoS_2 Nanoribbons

In this section, impact of gate voltage on electrical conductance of MoS_2 armchair nanoribbons has studied. For this purpose, three MoS_2 ACNR with different widths have been chosen; 3-ACNR, 4-ACNR and 10-ACNR. As explained in chapter three, transmission spectra of MoS_2 ACNRs comprise of three band gaps due to presence of electronic edge states. These three specific MoS_2 ACNRs have been chosen because of their distinctive transmission spectra profile. For 3-ACNR, there is a small gap at the center of transmission spectrum and at the negative energies (i.e. toward valence band) and a large gap at the positive energies (i.e. toward conduction band). For 4-ACNR, there is a small band gap at the center of transmission spectrum and at the positive energies, and there is a large band gap at the negative energies. For 10-ACNR, there is a large gap at the center of transmission spectrum and small gaps at both positive and negative energies. These properties are reflected in electrical conductance profile for each of these MoS_2 ACNRS as illustrated in Fig. 4.1. It can be seen from profile of electrical conductance that by increasing the magnitude of gate voltage in both polarities, electrical conductance increases. By further studying the Fig. 4.1, electrical conductance profile shifts toward valence band and conduction band for negative and positive gate voltages, respectively. It should be noted that by applying the gate voltage across the MoS_2 nanoribbons, there are two competing factors that shape up the impact of gate field on electrical conductance. The first effect is simply by accumulating the carriers at the

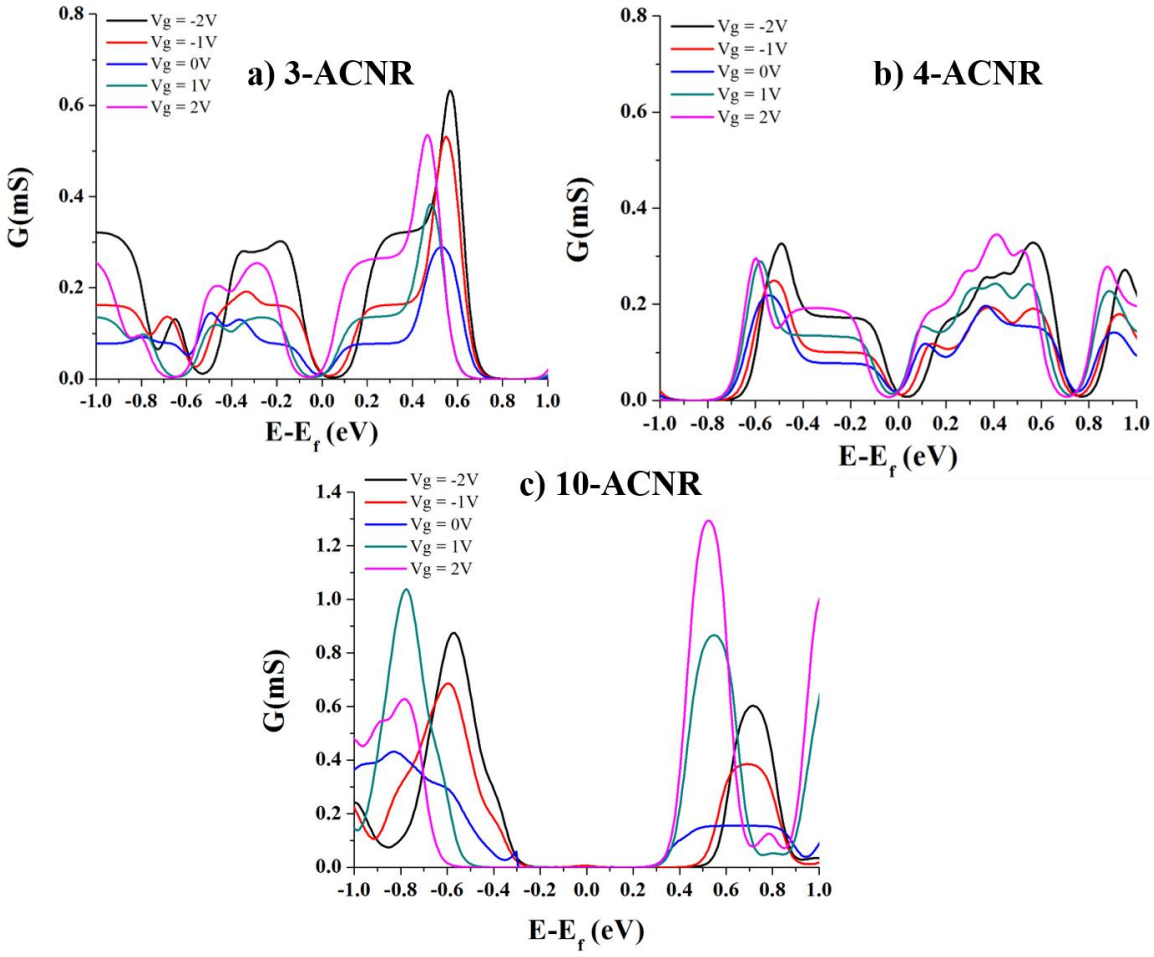

Figure 4.1: Electrical Conductance vs. energy as gate voltage changes for three different MoS_2 ACNRs; a) 3-ACNR, b) 4-ACNR and c) 10-ACNR.

surface of the MoS_2 ACNR and makes it more conductive and the other effect is surface boundary scattering. This phenomenon affects the mobility of the carriers when they are passing through the channel of the device. As the carriers are being conducted through the channel, they experience an electric field caused by imposing the gate voltage across the channel which attracts the carrier to surface, this attraction of carriers to the surface causes the carriers to scatter more and degrades the mobility and hence the electrical

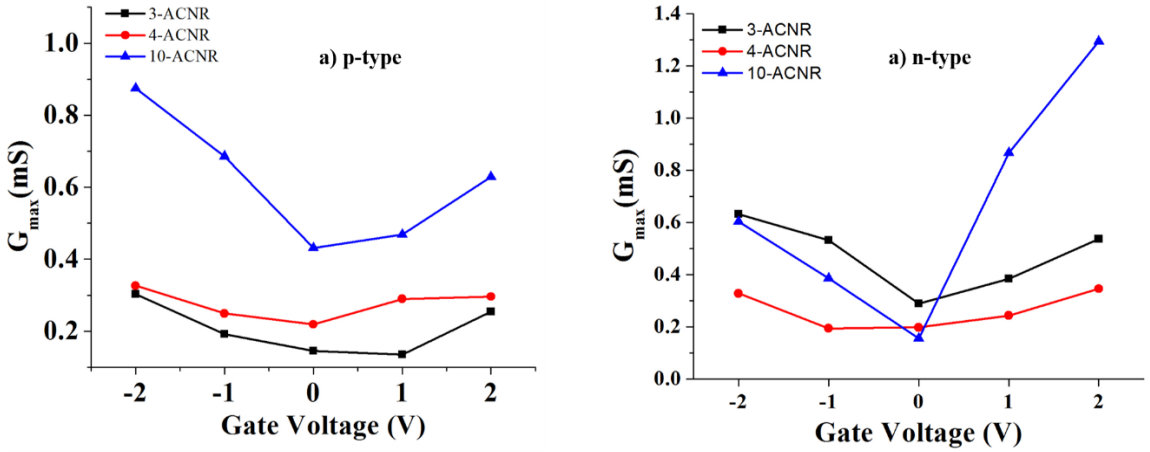

Figure 4.2: Maximum electrical conductance for MoS_2 ACNRs vs. gate voltage applied on them for a) holes and b) electrons

conductance. Maximum value of electrical conductance for both p-type (negative energies) and n-type (positive energies) regions is depicted in Fig. 4.2. In general, by applying negative gate voltage we expect to observe a more substantial increase in electrical conductance of p-type than n-type and by applying positive gate voltage we expect to see a more substantial increase in electrical conductance of n-type than p-type. For 10-ACNR, this is the case as it can be seen from Fig. 4.2, by applying positive gate bias, n-type maximum electrical conductance rises more sharply than p-type maximum electrical conductance and vice versa. For 3-ACNR and 4-ACNR, however, this is not the case. As gate voltage increases in its magnitude for both polarities, neither electrons nor holes electrical conductivity rises more substantially than the other. This phenomenon can be attributed to the size of the band gaps in electronic transmission spectra of these nanoribbons. For these two nanoribbons, 3-ACNR and 4-ACNR, the band gap at the middle of transmission spectrum is much smaller than the band gap at the middle of

transmission spectrum of 10-ACNR. This causes that by applying the gate voltage, regardless of its polarity, both the electrons and holes will contribute equally to the conductance.

4.3 Gate Impact on Seebeck Coefficient of MoS_2 Nanoribbons

In this section we study the effect of gate voltage on Seebeck coefficient. Framework for this study is the same as previous section. We accommodate three different MoS_2 ACNRS; 3-ACNR, 4-ACNR and 10-ACNR. Profile of Seebeck coefficient is illustrated for these MoS_2 ACNRS as a function of imposed gate voltage vs. Fermi level position in Fig. 4.3. It can be noted from the figure that as the gate electric field intensifies in both directions, the peak value of Seebeck coefficient decreases for all studied MoS_2 ACNRs. For positive gate voltages, Seebeck coefficient profile shifts toward left, aligning the positive peak of Seebeck coefficient on the fermi level. Positive peak of Seebeck coefficient corresponds to contribution of electrons to thermoelectric behavior. This is consistent with the fact that as more positive gate voltage we apply; the more electrons are populated at the surface of MoS_2 ACNR. The opposite happens for negative gate voltages. As more and more negative gate voltages are applied on the MoS_2 ACNR, the more Seebeck coefficient profile shifts toward right and aligning the negative peak of Seebeck coefficient profile on the Fermi level. Negative peak of Seebeck coefficient corresponds to contribution of hole to thermoelectric behavior. This is consistent to the fact that as more negative gate voltage we apply; the more holes are populated at the surface of MoS_2 ACNR. Another point that can be noted form Fig. 4.3 is that as a higher

positive gate voltage is imposed on the MoS_2 ACNR, the negative peak of Seebeck coefficient broadens and as a higher negative gate voltage is imposed on MoS_2 ACNR, the positive peak of Seebeck coefficient broadens. It has been already explained that the peak of Seebeck coefficient is dependent on the size of band gap and it reaches it

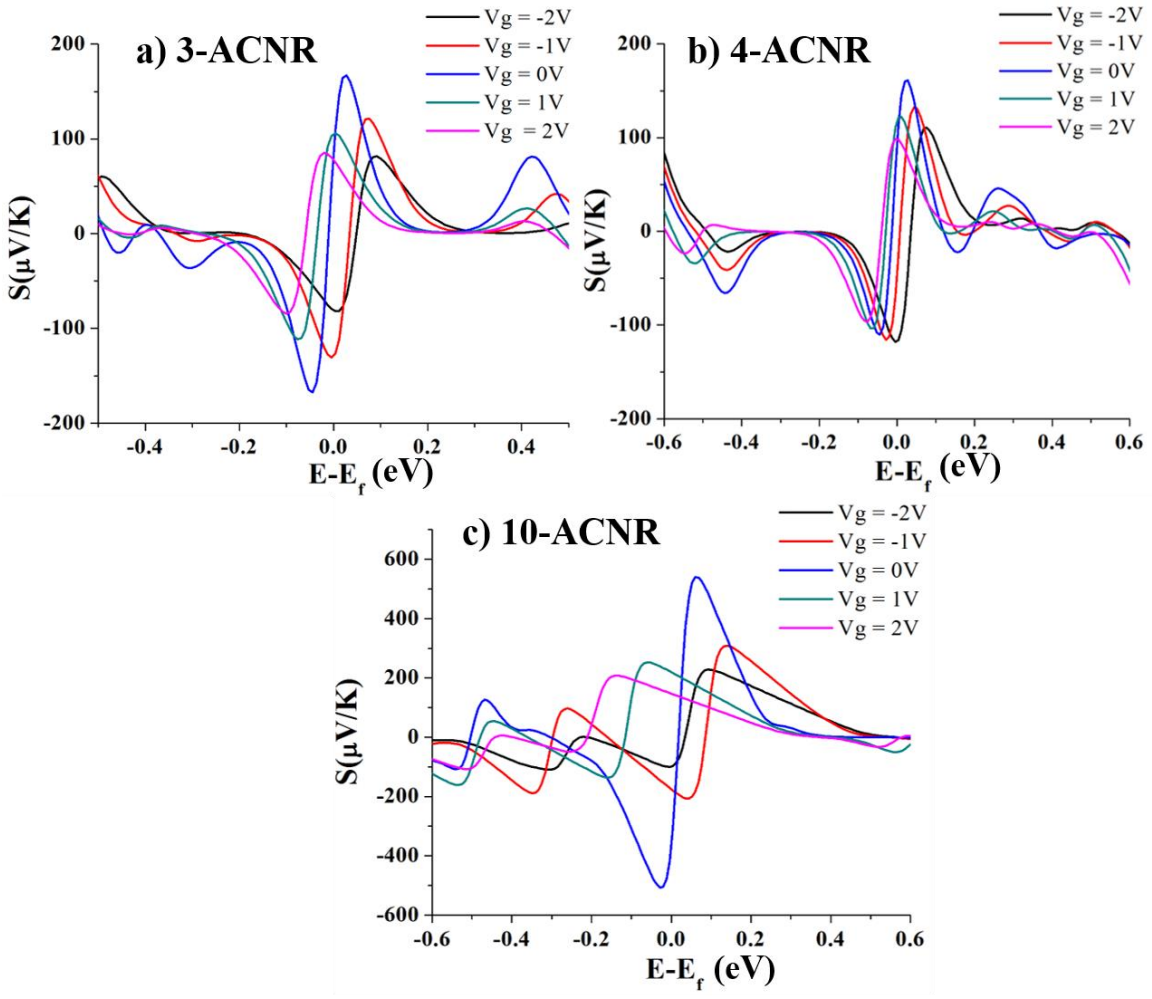

Figure 4.3: Seebeck coefficient of a) 3-ACNR, b) 4-ACNR and c) 10-ACNR as a function of gate voltage imposed across MoS_2 ACNR vs. position of Fermi level.

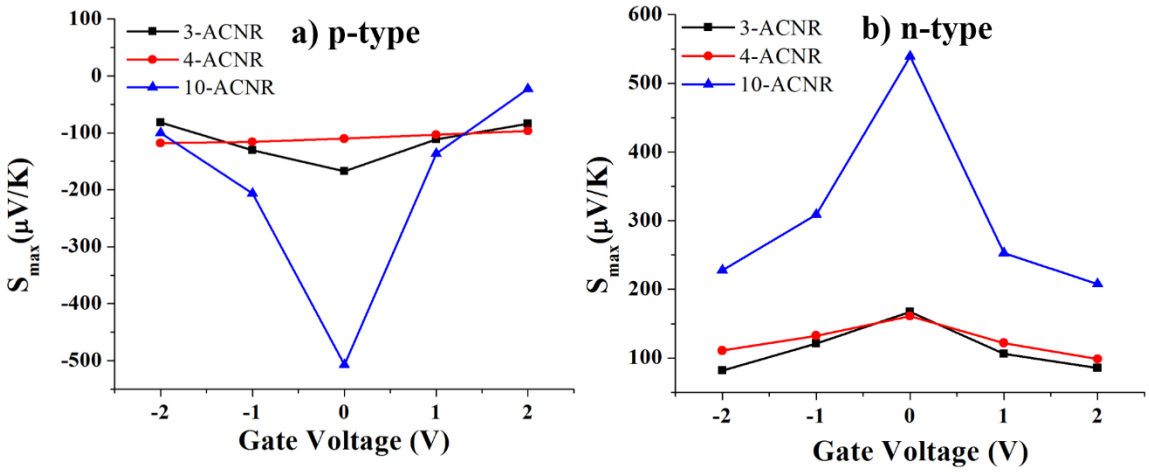

Figure 4.4: Seebeck coefficient peak value of MoS_2 ACNRs vs. applied gate voltage for a) p-type and b) n-type behaviors.

maximum values at energies close to conduction band or valence band edges. By applying a positive gate voltage, the quasi-fermi level approaches the edge of conduction band. As a result, it has a more distance toward the edge of valence band. So the Seebeck coefficients grows more slowly than when there was no gate voltage imposed and hence negative peak of Seebeck coefficient broadens. By applying a negative gate voltage, the quasi-fermi level approaches the edge of valence band. As a result, it has a more distance toward the edge of conduction band. So the Seebeck coefficients grows more slowly than when there was no gate voltage imposed and hence positive peak of Seebeck coefficient broadens. It can be seen from Fig. 4.3 that by increasing the gate voltage applied across MoS_2 ACNR, the peak value for p-type and n-type is decreasing. The peak value of Seebeck coefficient of MoS_2 ACNRs for both p-type and n-type is illustrated in Fig. 4.4. The change in peak value of Seebeck coefficient for 10-ACNR is much greater than the change in peak values of Seebeck coefficient in 3-ACNR and 4-ACNR. By imposing

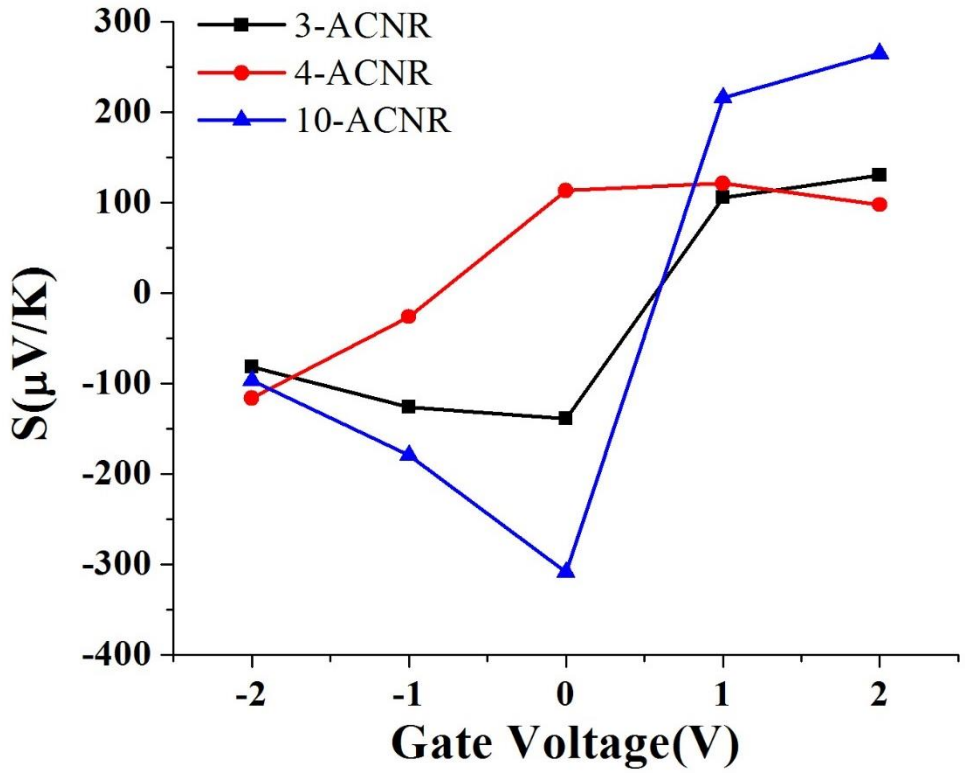

Figure 4.5: Value of Seebeck coefficient for different MoS_2 ACNRs vs. gate voltage

voltage across 10-ACNR, peak value of Seebeck coefficient drops to the level of Seebeck coefficient peak values of 3-ACNR and 4-ACNR. By increasing the amplitude of the gate voltage after initial voltage, drop date in Seebeck coefficient peak values decreases. This behavior can be explained by the fact that 10-ACNR has a much wider band gap at the center of its transmission spectrum in comparison with 3-ACNR and 4-ACNR. Having a wider gap than the other two MoS_2 ACNRs, imposing a gate voltage on 10-ACNR causes more tremendous change in free carriers and hence decreasing the peak value of Seebeck coefficient. In contrast to 10-ACNR, 3-ACNR and 4-ACNR has much smaller band gap

and has already lots of carriers and imposing gate voltage across them does not change carrier population significantly in comparison to initial gate bias across 10-ACNR. The value of Seebeck coefficient at zero fermi level shift vs. the gate voltage imposed across MoS_2 ACNRs, is depicted in Fig. 5.5, this figure illustrates the value of Seebeck coefficient without any fermi level shift. In other words, the Seebeck coefficient for MoS_2 ACNRs under the gate bias as is, without any need for doping the nanoribbon. At Zero gate bias 3-ACNR and 10-ACNR have negative Seebeck coefficients which means that holes contribute more to thermoelectric effect than electrons in contrast to 4-ACNR which has positive Seebeck coefficient at zero gate bias denoting that electrons contribute more than holes to thermoelectric behavior. By applying a positive gate voltage, Seebeck coefficient becomes positive for 10-ACNR and 3-ACNR and increases as gate voltage increase. For 4-ACNR, by applying a positive gate voltage Seebeck coefficient does not change and remain more or less constant. By applying negative gate voltage, Seebeck coefficient at fermi energy for 10-ACNR and 4-ACNR decrease in magnitude but remains negative and for 3-ACNR, Seebeck coefficient becomes negative and decreases as more negative gate voltage is imposed.

4.4 Gate Impact on Thermoelectric Figure of Merit of MoS2 Nanoribbons

In previous two sections, impact of imposing a gate voltage across MoS_2 ACNRs on their electrical conductance and Seebeck coefficient has been studied. As explained previously, these two parameters are heavily dependent on each other and an increase in

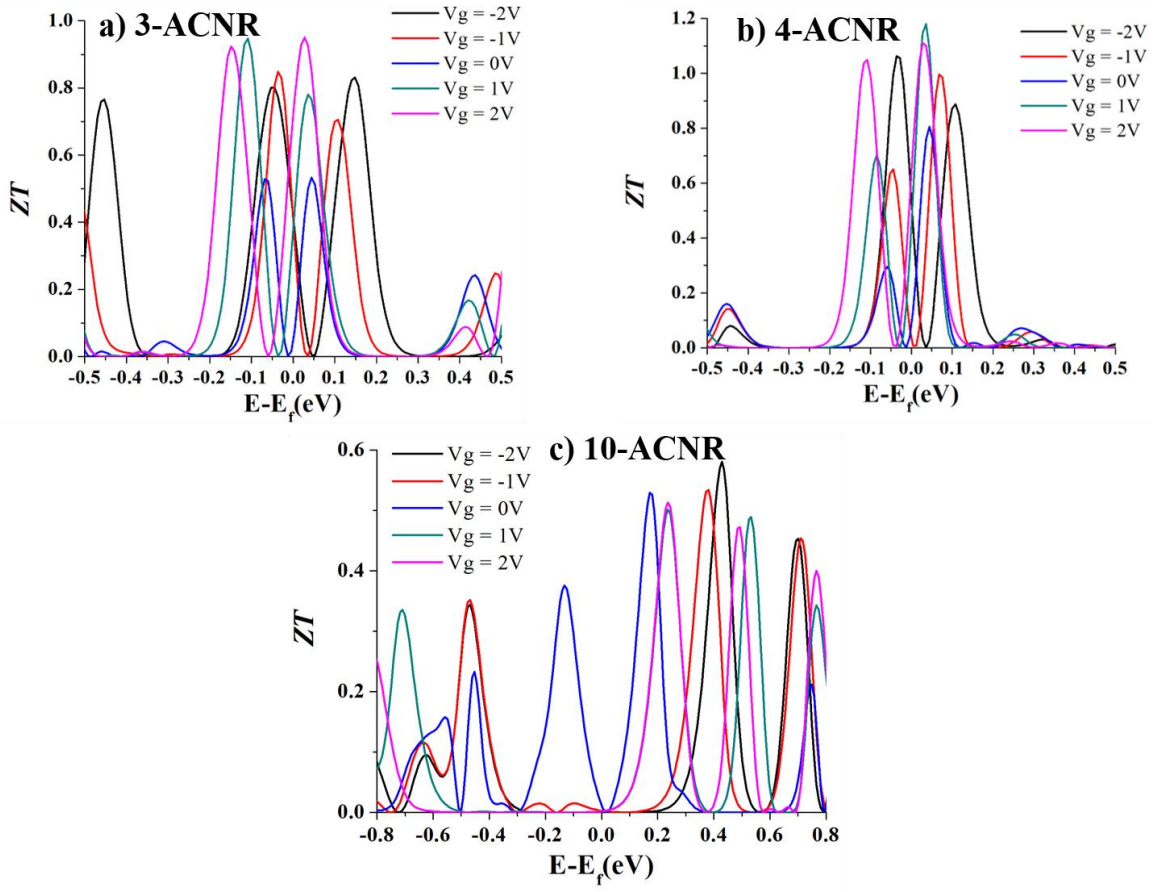

Figure 4.6: ZT vs. fermi level position in various MoS_2 ACNRs as a function of gate voltage imposed across the nanoribbons.

one of them is followed by decrease in the other. It is easier to describe this behavior by explaining it with respect to carrier concentration. As more gate voltage is imposed across MoS_2 ACNR, the more carriers are populated at the surface of nanoribbon and hence electrical conductance is increased. In contrast, it is well-known that by increasing the carrier concentration, Seebeck coefficient decreases. As a result, imposing a gate voltage has two contradictory impacts on thermoelectric figure of merit of the nanoribbon. Thermoelectric figure of merit is dependent on electrical conductance and

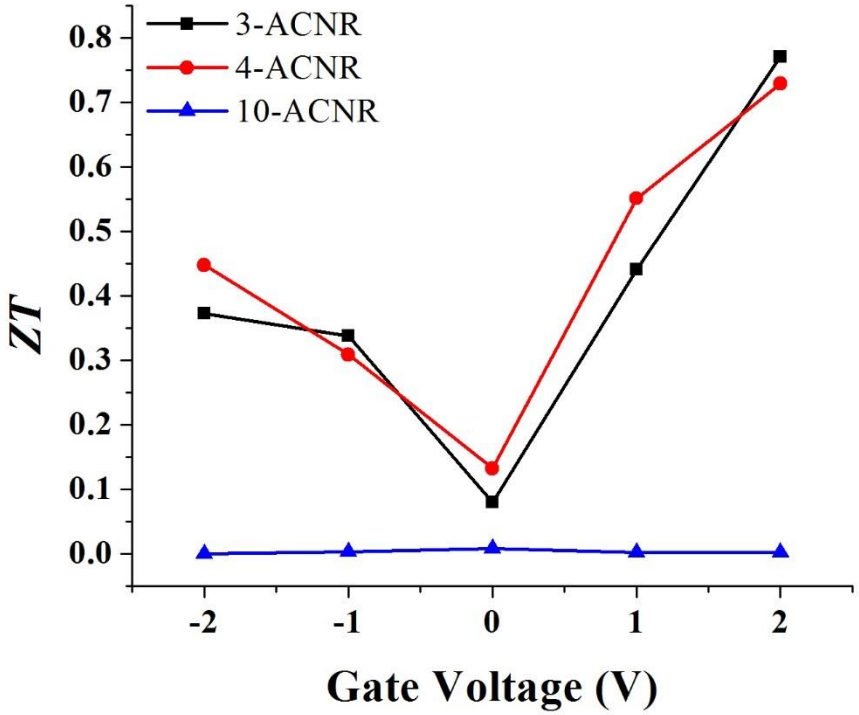

Figure 4.7: Value of thermoelectric figure of merit at zero fermi energy shift vs. the gate voltage imposed across MoS_2 ACNRs.

Seebeck coefficient in the form of S^2G, also known as power factor. Power factor has a parabolic profile vs. the carrier concentration and reaches its maximum at some optimized carrier concentration. So there would be a corresponding optimized gate voltage at which thermoelectric figure of merit reaches its maximum.

Thermoelectric figure of merit for these three MoS_2 ACNRs a function of gate bias vs. fermi level shift is depicted in Fig. 4.6. By imposing a positive gate voltage, similar to the case for Seebeck coefficient, ZT profile shifts to the left, indicating more contribution of electrons in thermoelectric effect than holes. By imposing negative gate voltage, ZT

profile shifts toward right, indicating more contribution from holes than electrons in thermoelectric effect. This mechanism is not very obvious in the case of MoS_2 10-ACNR. The reason for that is the fact that although by increasing the gate voltage, electrical conductance increases but its impact on thermoelectric figure of merit is more than compensated by sharp decrease in Seebeck coefficient as gate voltage increases. In contrast in the case of 3-ACNR and 4-ACNR, the drop in Seebeck coefficient is not as significant as in 10-ACNR and hence it does not have an impact on nullifying the effect of increase in electrical conductance. The value of thermoelectric figure of merit, ZT, at zero fermi level shift for MoS_2 ACNRs vs. function of gate voltage imposed on the nanoribbons is plotted in Fig. 4.7. As it can be noted, for 3-ACNR and 4-ACNR imposing a gate voltage across the nanoribbons increases the thermoelectric figure of merit that can be achieved without any doping. This is not the case for 10-ACNR as imposing gate voltage does not improve thermoelectric performance in hands without any doping.

4.5 Conclusion

Significant amount of fermi level shift was required to take advantage of high thermoelectric figure of merit of sheets of MoS_2. This caveat was addresses in chapter three by studying the thermoelectric behavior of MoS_2 ACNRs. In chapter four of this dissertation we tried to push more in order to address this caveat by imposing gate voltage on MoS_2 ACNRs. It was shown that by applying a gate voltage, there are two

competing effects on thermoelectric properties of MoS_2 ACNRs. First is that by applying a gate voltage, more carriers are being populated at the surface of nanoribbon and electrical conductance increases. In contrary, by populating more carriers, Seebeck coefficient decreases. Profile of ZT depends on product of these two parameters in form of S^2G, known as power factor, that reaches its maximum as some optimized carrier concentration and hence some optimized gate voltage. It was shown that, applying gate was useful in the case of 3-ACNR and 4-ACNR, which drop in Seebeck coefficient was more than compensated by increase in electrical conductance. But for 10-ACNR, this was not the case as the sharp drop in Seebeck coefficient by applying gate voltage, resulted in decrease in thermoelectric figure of merit.

CHAPTER FIVE: CONCLUSION AND FUTURE WORK

5.1 Conclusion

In chapter two of this dissertation, thermoelectric properties of mono-, bi-, tri- and quad-layer MoS_2 in both armchair and zigzag direction has been studied for electricity generation. It was found that as the number of layer increases from mono-layer to quad-layer, both transmission spectrum and phonon thermal conductance increase. In addition, strong electronic and thermal transport anisotropy is found between zigzag and armchair orientations. Transmission coefficient and phonon thermal conductivity of zigzag orientation is higher than those of armchair with the same number of layers. Their effect on ZT has been studied in this part. Results indicate that by increasing number of layers, ZT value tend to decrease. This behavior was in contrast to the fact that fewlayer MoS_2 is more conductive to monolayer in both directions and can be explained by suppression of out-of-plane vibrational mode in monolayer structure. Among all structures studied, monolayer armchair-oriented MoS_2 is shown to have the highest ZT value as both n-type and p-type semiconducting legs. Also, thermoelectric conversion of silicon thin films thermoelectric generator with the same thickness as MoS_2 armchair mono- and few-layer thermoelectric generator has been studied by using Synopsys TCAD software. The comparison indicated that proposed MoS_2 generator exhibits superior thermoelectric conversion efficiency.

In chapter three, we have studied thermoelectric properties of monolayer MoS_2 armchair nanoribbons. These nanoribbons are identified by number of zigzag chains across the ribbon denoted as N-ACNR. The effect of the size of nanoribbons on their thermoelectric behavior by considering N = 3-10 has been studied. Transmission spectra of ACNRs are comprised of edge states for both electrons and holes. This leads to existence of three gaps in transmission spectra. AS the width of the nanoribbon increases, the Seebeck coefficient and ZT at the center gap also increases. Phonon thermal conductance decreases by narrowing down the nanoribbons due to an increased impact of phonon edge scattering on overall phonon thermal conductance. As a result, the maximum ZT values that can be achieved by narrow ACNRs are higher than the wider ones. The effect of sulfur vacancy and edge roughness on thermoelectric properties is also studied. It is found that, although edge roughness will decrease phonon thermal conductance, the degradation in electrical conductance leads to a tremendous drop in *ZT*. In contrast to edge roughness, a sulfur vacancy decreases phonon thermal conductance without degrading electrical conductance as much as edge roughness, leading to an increased *ZT* value at some energies. It has been shown that *ZT* value as high as $ZT = 4$ in 3-ACNR for n-type material and $ZT = 3$ in 4-ACNR for p-type material at $T = 500K$ can be achieved. Possibility of gaining high *ZT* values for both n-type and p-type material makes monolayer MoS_2 ACNRs a promising candidate in future thermoelectric generators.

Significant amount of fermi level shift was required to take advantage of high thermoelectric figure of merit of sheets of MoS_2. This caveat was addresses in chapter

three by studying the thermoelectric behavior of MoS_2 ACNRs. In chapter four of this dissertation we tried to push more in order to address this caveat by imposing gate voltage on MoS_2 ACNRs. It was shown that by applying a gate voltage, there are two competing effects on thermoelectric properties of MoS_2 ACNRs. First is that by applying a gate voltage, more carriers are being populated at the surface of nanoribbon and electrical conductance increases. In contrary, by populating more carriers, Seebeck coefficient decreases. Profile of ZT depends on product of these two parameters in form of S^2G, known as power factor, that reaches its maximum as some optimized carrier concentration and hence some optimized gate voltage. It was shown that, applying gate was useful in the case of 3-ACNR and 4-ACNR, which drop in Seebeck coefficient was more than compensated by increase in electrical conductance. But for 10-ACNR, this was not the case as the sharp drop in Seebeck coefficient by applying gate voltage, resulted in decrease in thermoelectric figure of merit.

5.2 Future Work

There are some obstacles in better understanding thermoelectric properties of the rich family of 2D TMDCs on both theoretical and experimental ends. In theoretical domain, there are some issues that makes progress a lot more difficult. Lack of tight-binding parameters for these family of materials, makes it impossible to use fast tight-binding methods to study large system of atoms. Also lack of classical or semi-classical methods to model the vibrational mode of the lattice, makes it impossible to calculate phonon thermal properties of these materials easily. In addition to these lack of tools, there are

other aspects of thermoelectric generation that need to be studied. One of the most important of these areas is to find the perfect contact to inject the electron and hole ballistically into the channel. Study of different metals in contact to the channel and how the bonds form between MoS_2 and metal atoms can be of interest in designing the potential thermoelectric generators based on TMDCs.

In experimental end, the main obstacle in achieving potential thermoelectric generator based on this family of materials is to develop a reproducible growth mechanism to have a large scale and single crystalline layers of these materials. There are some advances on producing large-scale high-quality MoS_2 films but the recipes are not corroborated. Most of studies on these materials are on exfoliated flakes which is not a well-suited system for scaling up the production. The other missing knowledge is the fabrication knowledge and well-defined fabrication recipe. Due to ultra-thin body of these materials, any unwanted residual on the surface of these films can cause tremendous degradation in the material's property. All of these caveats should be addressed before one can realize the great thermoelectric potential of these materials.

BIBLIOGRAPHY

1. Goldsmid, H. *Thermoelectric refrigeration*. (Springer, 2013).
2. Morelli, D. T. *et al.* Low-temperature transport properties of p-type CoSb 3. *Phys. Rev. B* **51,** 9622 (1995).
3. Caillat, T., Borshchevsky, A. & Fleurial, J.-P. Properties of single crystalline semiconducting CoSb3. *J. Appl. Phys.* **80,** 4442–4449 (1996).
4. Nolas, G. S., Morelli, D. T. & Tritt, T. M. Skutterudites: A phonon-glass-electron crystal approach to advanced thermoelectric energy conversion applications. *Annu. Rev. Mater. Sci.* **29,** 89–116 (1999).
5. Hicks, L. D., Harman, T. C., Sun, X. & Dresselhaus, M. S. Experimental study of the effect of quantum-well structures on the thermoelectric figure of merit. *Phys. Rev. B* **53,** R10493 (1996).
6. Rowe, D. M. *Thermoelectrics handbook: macro to nano*. (CRC press, 2005).
7. Chen, G. Thermal conductivity and ballistic-phonon transport in the cross-plane direction of superlattices. *Phys. Rev. B* **57,** 14958 (1998).
8. Springholz, G., Holy, V., Pinczolits, M. & Bauer, G. Self-organized growth of three-dimensional quantum-dot crystals with fcc-like stacking and a tunable lattice constant. *Science* **282,** 734–737 (1998).
9. Springholz, G. *et al.* Tuning of vertical and lateral correlations in self-organized PbSe/Pb 1- x Eu x Te quantum dot superlattices. *Phys. Rev. Lett.* **84,** 4669 (2000).
10. Harman, T. C., Walsh, M. P., Turner, G. W. & others. Nanostructured thermoelectric materials. *J. Electron. Mater.* **34,** L19–L22 (2005).
11. Harman, T. C., Taylor, P. J., Walsh, M. P. & LaForge, B. E. Quantum dot superlattice thermoelectric materials and devices. *science* **297,** 2229–2232 (2002).

12. Harman, T. C., Taylor, P. J., Spears, D. L. & Walsh, M. P. Thermoelectric quantum-dot superlattices with high ZT. *J. Electron. Mater.* **29,** L1–L2 (2000).
13. Yang, R. & Chen, G. Thermal conductivity modeling of periodic two-dimensional nanocomposites. *Phys. Rev. B* **69,** 195316 (2004).
14. Abeles, B. Lattice thermal conductivity of disordered semiconductor alloys at high temperatures. *Phys. Rev.* **131,** 1906 (1963).
15. Rosi, F. D. Thermoelectricity and thermoelectric power generation. *Solid-State Electron.* **11,** 833–868 (1968).
16. Kuznetsov, V. L., Kuznetsova, L. A., Kaliazin, A. E. & Rowe, D. M. High performance functionally graded and segmented Bi2Te3-based materials for thermoelectric power generation. *J. Mater. Sci.* **37,** 2893–2897 (2002).
17. KANG, C., WANG, H., BAHK, J.-H., KIMa, H. & KIM, W. Thermoelectric Materials and Devices. *Hierarchical Nanostructures Energy Devices* 107 (2014).
18. Gelbstein, Y., Dashevsky, Z. & Dariel, M. P. High performance n-type PbTe-based materials for thermoelectric applications. *Phys. B Condens. Matter* **363,** 196–205 (2005).
19. Novoselov, K. S. *et al.* Two-dimensional atomic crystals. *Proc. Natl. Acad. Sci. U. S. A.* **102,** 10451–10453 (2005).
20. Ferrari, A. C. *et al.* Raman spectrum of graphene and graphene layers. *Phys. Rev. Lett.* **97,** 187401 (2006).
21. Novoselov, K. S. A. *et al.* Two-dimensional gas of massless Dirac fermions in graphene. *nature* **438,** 197–200 (2005).
22. Frindt, R. F. Single crystals of MoS2 several molecular layers thick. *J. Appl. Phys.* **37,** 1928–1929 (1966).
23. Schumacher, A., Scandella, L., Kruse, N. & Prins, R. Single-layer MoS 2 on mica: studies by means of scanning force microscopy. *Surf. Sci.* **289,** L595–L598 (1993).
24. Li, Y., Zhou, Z., Zhang, S. & Chen, Z. MoS2 nanoribbons: high stability and unusual electronic and magnetic properties. *J. Am. Chem. Soc.* **130,** 16739–16744 (2008).

25. Kou, L. *et al.* Tuning magnetism and electronic phase transitions by strain and electric field in zigzag MoS2 nanoribbons. *J. Phys. Chem. Lett.* **3,** 2934–2941 (2012).
26. Ataca, C., Sahin, H., Akturk, E. & Ciraci, S. Mechanical and electronic properties of MoS2 nanoribbons and their defects. *J. Phys. Chem. C* **115,** 3934–3941 (2011).
27. Kam, K. K. & Parkinson, B. A. Detailed photocurrent spectroscopy of the semiconducting group VIB transition metal dichalcogenides. *J. Phys. Chem.* **86,** 463–467 (1982).
28. Mak, K. F., Lee, C., Hone, J., Shan, J. & Heinz, T. F. Atomically thin MoS 2: a new direct-gap semiconductor. *Phys. Rev. Lett.* **105,** 136805 (2010).
29. Radisavljevic, B., Radenovic, A., Brivio, J., Giacometti, V. & Kis, A. Single-layer MoS2 transistors. *Nat. Nanotechnol.* **6,** 147–150 (2011).
30. Gourmelon, E., Bernede, J. C., Pouzet, J. & Marsillac, S. Textured MoS2 thin films obtained on tungsten: Electrical properties of the W/MoS2 contact. *J. Appl. Phys.* **87,** 1182–1186 (2000).
31. Radisavljevic, B., Whitwick, M. B. & Kis, A. Integrated circuits and logic operations based on single-layer MoS2. *ACS Nano* **5,** 9934–9938 (2011).
32. Yu, S., Eshun, K., Zhu, H. & Li, Q. Novel Two-Dimensional Mechano-Electric Generators and Sensors Based on Transition Metal Dichalcogenides. *Sci. Rep.* **5,** (2015).
33. Kuc, A., Zibouche, N. & Heine, T. Influence of quantum confinement on the electronic structure of the transition metal sulfide T S 2. *Phys. Rev. B* **83,** 245213 (2011).
34. Pei, Y., LaLonde, A., Iwanaga, S. & Snyder, G. J. High thermoelectric figure of merit in heavy hole dominated PbTe. *Energy Environ. Sci.* **4,** 2085–2089 (2011).
35. Biswas, K. *et al.* High-performance bulk thermoelectrics with all-scale hierarchical architectures. *Nature* **489,** 414–418 (2012).
36. Hicks, L. D. & Dresselhaus, M. S. Effect of quantum-well structures on the thermoelectric figure of merit. *Phys. Rev. B* **47,** 12727 (1993).
37. Hicks, L. D. & Dresselhaus, M. S. Thermoelectric figure of merit of a one-dimensional conductor. *Phys. Rev. B* **47,** 16631 (1993).

38. Dresselhaus, M. S. *et al.* New Directions for Low-Dimensional Thermoelectric Materials. *Adv. Mater.* **19,** 1043–1053 (2007).

39. Rowe, D. M., Shukla, V. S. & Savvides, N. Phonon scattering at grain boundaries in heavily doped fine-grained silicon–germanium alloys. (1981).

40. Hochbaum, A. I. *et al.* Enhanced thermoelectric performance of rough silicon nanowires. *Nature* **451,** 163–167 (2008).

41. Shi, X., Chen, L., Yang, J. & Meisner, G. P. Enhanced thermoelectric figure of merit of CoSb3 via large-defect scattering. *Appl. Phys. Lett.* **84,** 2301 (2004).

42. Mansfield, R. & Salam, S. A. Electrical properties of molybdenite. *Proc. Phys. Soc. Sect. B* **66,** 377 (1953).

43. Buscema, M. *et al.* Large and tunable photothermoelectric effect in single-layer MoS2. *Nano Lett.* **13,** 358–363 (2013).

44. Liu, X., Zhang, G., Pei, Q.-X. & Zhang, Y.-W. Phonon thermal conductivity of monolayer MoS2 sheet and nanoribbons. *Appl. Phys. Lett.* **103,** 133113 (2013).

45. Jiang, J.-W., Park, H. S. & Rabczuk, T. Molecular dynamics simulations of single-layer molybdenum disulphide (MoS2): Stillinger-Weber parametrization, mechanical properties, and thermal conductivity. *J. Appl. Phys.* **114,** 64307 (2013).

46. Huai-Hong, G., Teng, Y., Peng, T. & Zhi-Dong, Z. Theoretical study of thermoelectric properties of MoS2. *Chin. Phys. B* **23,** 17201 (2014).

47. Agarwal, M. K. & Talele, L. T. Transport properties of molybdenum sulphoselenide (MoS x Se 2-x, $0 \leqslant x \leqslant 2$) single crystals. *Solid State Commun.* **59,** 549–551 (1986).

48. Thakurta, S. G. & Dutta, A. K. Electrical conductivity, thermoelectric power and hall effect in p-type molybdenite (MoS 2) crystal. *J. Phys. Chem. Solids* **44,** 407–416 (1983).

49. Guo, H., Yang, T., Tao, P., Wang, Y. & Zhang, Z. High pressure effect on structure, electronic structure, and thermoelectric properties of MoS2. *J. Appl. Phys.* **113,** 13709 (2013).

50. Jiang, J.-W., Zhuang, X. & Rabczuk, T. Orientation dependent thermal conductance in single-layer MoS2. *Sci. Rep.* **3,** (2013).

51. Li, Q. *et al.* Molybdenum disulfide nanowires and nanoribbons by electrochemical/chemical synthesis. *J. Phys. Chem. B* **109,** 3169–3182 (2005).

52. Li, Q., Newberg, J. T., Walter, E. C., Hemminger, J. C. & Penner, R. M. Polycrystalline molybdenum disulfide (2H-MoS2) nano-and microribbons by electrochemical/chemical synthesis. *Nano Lett.* **4,** 277–281 (2004).

53. Liu, X. *et al.* Top–down fabrication of sub-nanometre semiconducting nanoribbons derived from molybdenum disulfide sheets. *Nat. Commun.* **4,** 1776 (2013).

54. Lin, Y.-C. *et al.* Wafer-scale MoS 2 thin layers prepared by MoO 3 sulfurization. *Nanoscale* **4,** 6637–6641 (2012).

55. Song, I. *et al.* Patternable Large-Scale Molybdenium Disulfide Atomic Layers Grown by Gold-Assisted Chemical Vapor Deposition. *Angew. Chem. Int. Ed.* **53,** 1266–1269 (2014).

56. Najmaei, S. *et al.* Vapour phase growth and grain boundary structure of molybdenum disulphide atomic layers. *Nat. Mater.* **12,** 754–759 (2013).

57. van der Zande, A. M. *et al.* Grains and grain boundaries in highly crystalline monolayer molybdenum disulphide. *Nat. Mater.* **12,** 554–561 (2013).

58. Kang, K. *et al.* High-mobility three-atom-thick semiconducting films with wafer-scale homogeneity. *Nature* **520,** 656–660 (2015).

59. Brandbyge, M., Mozos, J.-L., Ordejón, P., Taylor, J. & Stokbro, K. Density-functional method for nonequilibrium electron transport. *Phys. Rev. B* **65,** 165401 (2002).

60. Büttiker, M., Imry, Y., Landauer, R. & Pinhas, S. Generalized many-channel conductance formula with application to small rings. *Phys. Rev. B* **31,** 6207 (1985).

61. Monkhorst, H. J. & Pack, J. D. Special points for Brillouin-zone integrations. *Phys. Rev. B* **13,** 5188 (1976).

62. Datta, S. *Quantum transport: atom to transistor*. (Cambridge University Press, 2005).

63. Stillinger, F. H. & Weber, T. A. Computer simulation of local order in condensed phases of silicon. *Phys. Rev. B* **31,** 5262 (1985).

64. Li, Y., Zhou, Z., Zhang, S. & Chen, Z. MoS2 nanoribbons: High stability and unusual electronic and magnetic properties. *J. Am. Chem. Soc.* **130,** 16739–16744 (2008).

65. Ataca, C., Sahin, H., Akturk, E. & Ciraci, S. Mechanical and electronic properties of MoS2 nanoribbons and their defects. *J. Phys. Chem. C* **115,** 3934–3941 (2011).

66. Kou, L. *et al.* Tuning Magnetism and Electronic Phase Transitions by Strain and Electric Field in Zigzag MoS2 Nanoribbons. *J. Phys. Chem. Lett.* **3,** 2934–2941 (2012).

67. Das, S. & Appenzeller, J. Screening and interlayer coupling in multilayer MoS2. *Phys. Status Solidi RRL-Rapid Res. Lett.* **7,** 268–273 (2013).

68. Jiang, J.-W., Zhuang, X. & Rabczuk, T. Orientation Dependent Thermal Conductance in Single-Layer MoS2. *Sci. Rep.* **3,** (2013).

69. Huang, W., Da, H. & Liang, G. Thermoelectric performance of MX2 (M= Mo, W; X= S, Se) monolayers. *J. Appl. Phys.* **113,** 104304 (2013).

70. Dresselhaus, M. S. *et al.* New Directions for Low-Dimensional Thermoelectric Materials. *Adv. Mater.* **19,** 1043–1053 (2007).

71. Komsa, H.-P. *et al.* Two-dimensional transition metal dichalcogenides under electron irradiation: defect production and doping. *Phys. Rev. Lett.* **109,** 35503 (2012).

72. Dolui, K., Rungger, I., Pemmaraju, C. D. & Sanvito, S. Possible doping strategies for MoS 2 monolayers: An ab initio study. *Phys. Rev. B* **88,** 75420 (2013).

73. Yue, Q., Chang, S., Qin, S. & Li, J. Functionalization of monolayer MoS 2 by substitutional doping: a first-principles study. *Phys. Lett. A* **377,** 1362–1367 (2013).

74. Eshun, K., Xiong, H. D., Yu, S. & Li, Q. Doping induces large variation in the electrical properties of MoS 2 monolayers. *Solid-State Electron.* **106,** 44–49 (2015).

75. Cai, Y., Zhang, G. & Zhang, Y.-W. Polarity-reversed robust carrier mobility in monolayer MoS2 nanoribbons. *J. Am. Chem. Soc.* **136,** 6269–6275 (2014).

76. Pan, H. & Zhang, Y.-W. Edge-dependent structural, electronic and magnetic properties of MoS 2 nanoribbons. *J. Mater. Chem.* **22,** 7280–7290 (2012).

77. Botello-Méndez, A. R., Lopez-Urias, F., Terrones, M. & Terrones, H. Metallic and ferromagnetic edges in molybdenum disulfide nanoribbons. *Nanotechnology* **20,** 325703 (2009).

78. Zheng, H., Wang, Z. F., Luo, T., Shi, Q. W. & Chen, J. Analytical study of electronic structure in armchair graphene nanoribbons. *Phys. Rev. B* **75,** 165414 (2007).

79. Pan, L. *et al.* Thermoelectric properties of armchair and zigzag silicene nanoribbons. *Phys. Chem. Chem. Phys.* **14,** 13588–13593 (2012).

80. Ouyang, Y. & Guo, J. A theoretical study on thermoelectric properties of graphene nanoribbons. *Appl. Phys. Lett.* **94,** 263107 (2009).

81. Jiang, J.-W., Wang, J.-S. & Li, B. A nonequilibrium Green's function study of thermoelectric properties in single-walled carbon nanotubes. *J. Appl. Phys.* **109,** 14326 (2011).

82. Guo, Z., Zhang, D. & Gong, X.-G. Thermal conductivity of graphene nanoribbons. *Appl. Phys. Lett.* **95,** 163103 (2009).

83. Arab, A. & Li, Q. Anisotropic thermoelectric behavior in armchair and zigzag mono-and fewlayer MoS2 in thermoelectric generator applications. *Sci. Rep.* **5,** (2015).

BIOGRAPHY

Abbas Arab received his Bachelor of Science in Electrical and Computer Engineering program from AmirKabir University in Tehran, Iran in 2009. He continued his study pursuing his Master of Science in Electrical and Computer Engineering, minoring in nanoelectrocnics, from Sharif University of Technology in Tehran, Iran in 2011. He continued his study in pursuit of Ph.D. in Electrical and Computer Engineering program from George Mason University, Fairfax, Virginia. His research during his PhD study was focused on novel semiconducting low-dimensional materials and their applications in electronic and thermoelectric industry.